

Slush-like polar structures in single-crystal relaxors

Hiroyuki Takenaka¹, Ilya Grinberg^{1,2}, Shi Liu¹ & Andrew M. Rappe¹

Despite more than 50 years of investigation, it is still unclear how the underlying structure of relaxor ferroelectrics gives rise to their defining properties, such as ultrahigh piezoelectric coefficients, high permittivity over a broad temperature range, diffuse phase transitions, strong frequency dependence in dielectric response, and phonon anomalies^{1–10}. The model of polar nanoregions inside a non-polar matrix has been widely used to describe the structure of relaxor ferroelectrics¹¹. However, the lack of precise knowledge about the shapes, growth and dipole patterns of polar nanoregions has led to the characterization of relaxors as “hopeless messes”¹², and no predictive model for relaxor behaviour is currently available. Here we use molecular dynamics simulations of the prototypical $\text{Pb}(\text{Mg}_{1/3}\text{Nb}_{2/3})\text{O}_3\text{-PbTiO}_3$ relaxor material to examine its structure and the spatial and temporal polarization correlations. Our simulations show that the unusual properties of relaxors stem from the presence of a multi-domain state with extremely small domain sizes (2–10 nanometres), and no non-polar matrix, owing to the local dynamics. We find that polar structures in the multi-domain state in relaxors are analogous to those of the slush state of water. The multi-domain structure of relaxors that is revealed by our molecular dynamics simulations is consistent with recent experimental diffuse scattering results and indicates that relaxors have a high density of low-angle domain walls. This insight explains the recently discovered classes of relaxors¹³ that cannot be described by the polar nanoregion model, and provides guidance for the design and synthesis of new relaxor materials.

In Pb-based perovskites, relaxor behaviour has been known to arise from the presence of strong disorder and valence variation on the A and B sites of the perovskite solid solution. Since 1983, the model of polar nanoregions inside a non-polar matrix¹¹ has been used to explain the experimentally observed diffuse phase transitions (see Methods section ‘Polar nanoregion model’), with Burns T_b , intermediate T^* and freezing T_f phase transition temperatures ($T_b > T^* > T_f$) related to the appearance, growth and freezing-in of the polar nanoregions. However, this model is essentially a post hoc justification of the experimental results and has not been used predictively. Similarly, it cannot explain the relaxor behaviour that was recently observed in the P(VDF-TrFE-CTFE) ferroelectric terpolymer¹³.

Over the past two decades, many experimental studies have used diffuse scattering to probe relaxor behaviour, showing that diffuse scattering intensity is correlated with relaxor transition. In particular, the appearance of a butterfly shape in the diffuse scattering pattern was considered to be a structural signature of polar nanoregion and relaxor behaviour. However, recent diffuse scattering studies¹⁴ have questioned the validity of the polar nanoregion model, and the butterfly pattern was also observed in solid solutions of the ferroelectric $\text{Pb}(\text{Zr,Ti})\text{O}_3$ near the Curie temperature T_c , with the diffuse scattering intensity decaying rapidly on cooling^{15,16}. Here we use molecular dynamics simulations of $72 \times 72 \times 72$ unit cells of $0.75\text{Pb}(\text{Mg}_{1/3}\text{Nb}_{2/3})\text{O}_3\text{-}0.25\text{PbTiO}_3$ (PMN-PT), a relaxor for which we have an accurate atomistic model potential¹⁷. Our choice of this particular composition

is validated by comparing theoretical diffuse scattering to the experimental diffuse scattering for $(1-x)\text{Pb}(\text{Mg}_{1/3}\text{Nb}_{2/3})\text{O}_3\text{-}x\text{PbTiO}_3$ ($x=0, 0.1, 0.2$ or 0.3) relaxors¹⁸ (see Methods section ‘Diffuse scattering’). We provide a physical interpretation of the butterfly shape in the diffuse scattering pattern by analysing the correlations between the local off-centre displacements of Pb atoms (explained below and in Methods section ‘Diffuse scattering’). The analysis of the temperature dependence of displacement correlations provides a new, predictive model that explains the properties of relaxors.

The time-delay-averaged (over 2 ns) angle correlations for pairs of dipoles generated by displacements of Pb atoms from the centres of their O_{12} cages reveal the structure and dynamics of the relaxor phase and show that the butterfly shape is a signature of a multi-domain, disordered ferroelectric state with an extremely small domain size of 2–10 nm. We analyse the angles between Pb– O_{12} dipoles along the $\langle 100 \rangle$, $\langle 110 \rangle$ and $\langle 111 \rangle$ directions (see Methods section ‘Angle correlations’). To reveal the trends in the distance dependence of the Pb– O_{12} dipole correlations, we plot the peak of the angle distribution (most probable angle formed between Pb– O_{12} displacement pairs) versus distance, for several temperatures T (Fig. 1a). The flat curves at around 90° for $T=600$ K and $T=700$ K in the paraelectric phase indicate the lack of correlations, and overlap each other. At $T=500$ K $< T_b$, a weak distance dependence is found with the onset of a broad distribution. At $T=400$ K $< T^*$, the local dipoles start to form domains, as indicated by stronger correlations for distances less than about 6 nm. At lower T , there is a clear distinction between strong correlations for distances less than about 6 nm and weak correlations for larger distances. Direct visualization and analysis of the local polarization \mathbf{P} reveal a multi-domain state, with the weakly temperature-dependent domain size of 2–10 nm and low-angle ($55^\circ \pm 10^\circ$) changes in \mathbf{P} at the domain walls enabled by the small energy differences between the $\langle 100 \rangle$, $\langle 110 \rangle$ and $\langle 111 \rangle$ orientations of the local \mathbf{P} (Fig. 1b; see Methods section ‘Analysis of domain size’ for details). Thus, PMN-PT assumes a multi-domain state with various low-angle domain walls separating small polar domains, without a non-polar matrix. This result is unlike those of previous simulations¹⁹ of $\text{Pb}(\text{Sc,Nb})\text{O}_3$, in which case a mixture of B-cation ordered and disordered regions was studied and it was found¹⁹ that the dielectric response was driven by the ordered ferroelectric-like regions, identified as polar nanoregions, with the chemically imbalanced, disordered regions as the matrix. However, this model is inappropriate for PMN-PT, because PMN-PT lacks chemically imbalanced, large, B-cation disordered regions. In contrast to the previously accepted picture of polar nanoregion growth inside a non-polar matrix on cooling, the main changes during the transitions at T^* and T_f are the appearance of correlation inside the domains and reduced rotation of domain polarization, whereas the polar domain size grows only slightly. The growth of polar nanoregions, which is the key feature of the polar nanoregion model, is therefore unnecessary to reproduce relaxor behaviour²⁰.

To provide a conceptual picture of the structural changes through the phase transitions, we extend the analogy between relaxors and water¹⁷;

¹Department of Chemistry, University of Pennsylvania, Philadelphia, Pennsylvania 19104, USA. ²Department of Chemistry, Bar-Ilan University, Ramat Gan, Israel.

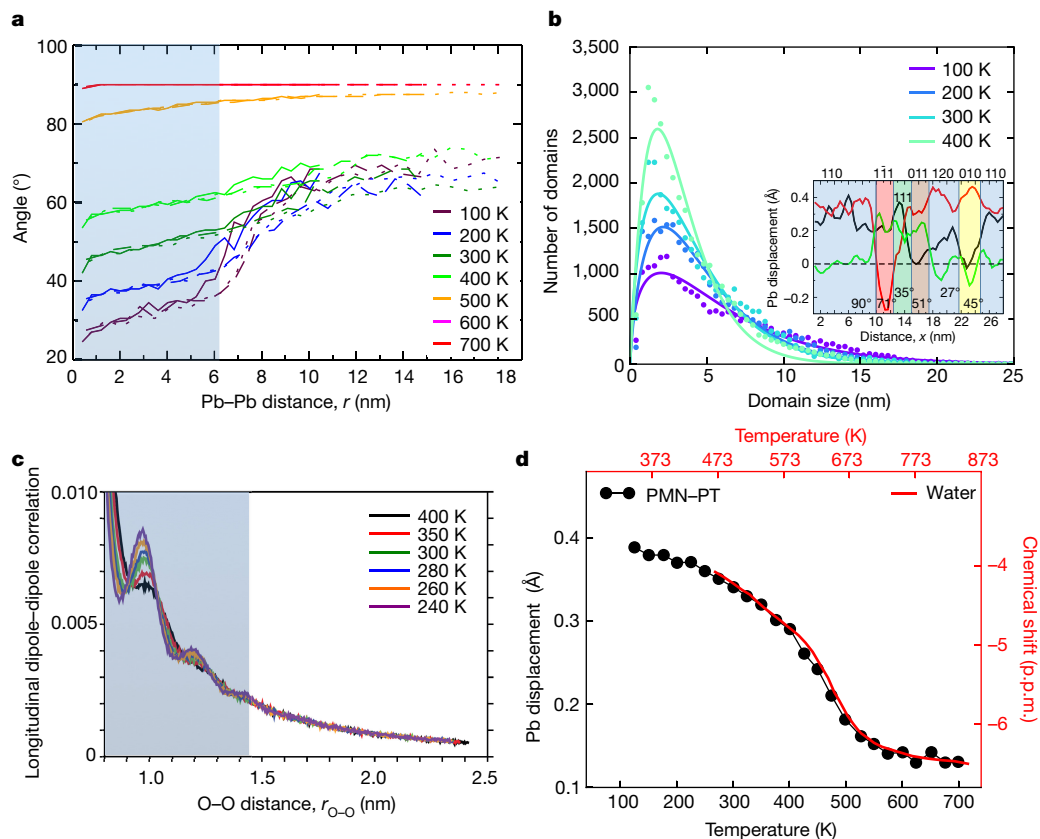


Figure 1 | Comparison of PMN-PT to water. **a**, Most probable angles (corresponding to the peak in the distribution of angles formed between Pb–O₁₂ displacement pairs) of the time-delay-averaged Pb–Pb angle correlations versus inter-atomic distance r for various temperatures T . Solid, dashed and dotted lines depict correlations along $\langle 100 \rangle$, $\langle 110 \rangle$ and $\langle 111 \rangle$, respectively. Separated by 60° and 6 nm at $T \leq 400\text{ K}$, two regions are apparent: temperature-independent weak correlation at higher r , and stronger correlation for smaller r . **b**, Domain-size distribution from molecular dynamics simulations of PMN-PT. Filled circles show the number of domains of a given size obtained from molecular dynamics snapshots; solid lines show fits of the data to Poisson distributions. The inset shows the off-centre displacements of the Pb atom in the k th unit cell along the x axis of the supercell ($k \in \{1, 2, \dots, 72\}$) as a function of the distance x from the first Pb atom in the supercell, taken from a molecular dynamics snapshot at $T = 100\text{ K}$. The black, red and green curves represent the x , y and z components of the displacements, respectively. The hkl indices given for each domain (indicated by differently coloured shading) correspond to \mathbf{P} directions derived from approximate ratios of the x , y and z components of the Pb displacements in each domain; the

this analogy is supported by the similarities in the dielectric response (see Methods section ‘Similarities of relaxors to water’). Comparison of our molecular dynamics results for PMN-PT and previous studies of water^{21–24} shows that, for water and relaxors, the transitions upon cooling from $T > T_b$ are characterized by the following features. (a) Small correlated regions without non-polar matrix (Fig. 2a) dynamically appear and move around at temperatures below T_b , resulting in weak time-delay-averaged correlations (Extended Data Fig. 8d–f), with rapid rotations of \mathbf{P} leading to random orientations in the whole PMN-PT system, similar to the weak water correlation peak that appears at around 1.2 nm at $T = 350\text{ K}$ (Fig. 1c), owing to the presence of random H bonds. (b) On cooling water from $T = 300\text{ K}$ or PMN-PT from T^* , the sizes of the correlated regions (approximately 1.5 nm in water and 6 nm in PMN-PT) are largely unchanged, with much stronger correlations inside the region boundaries (Fig. 1a, c) leading to increased average order in the material. (c) A distribution of different degrees of ordering is present at all T , but shifts towards greater order and slower dynamics with cooling (see below and in

Fig. 3). We also find that the temperature evolution of the magnitude of the local Pb displacements (experimentally available from inelastic neutron scattering) in PMN-PT¹⁷ resembles that of the ¹H NMR chemical shift in water under pressure²² (Fig. 1d); these properties can be considered to be order parameters. We propose that it is the presence of such fixed-size polar nanodomains that leads to the relaxor-like dielectric response, both in water and in Pb-based ABO₃ relaxors. The relaxor structure below T^* and T_f is characterized by strong but incomplete correlations inside the domains and weak correlations between the domains. These features are due to the mixture of unit cells with ferroelectric- and paraelectric-like behaviour (as explained below), as was shown for B-cation-centred dipoles²⁵. The incomplete correlation enables collective polarization rotations of the dipoles in each individual domain, leading to slow rotations of domain \mathbf{P} . This behaviour is similar to that of slush water around the melting temperature, which is a slurry-like mixture of small ice crystals and liquid water²⁶; in this state, the dynamics of the molecules inside the crystalline regions are slow, whereas the dynamics of the molecules

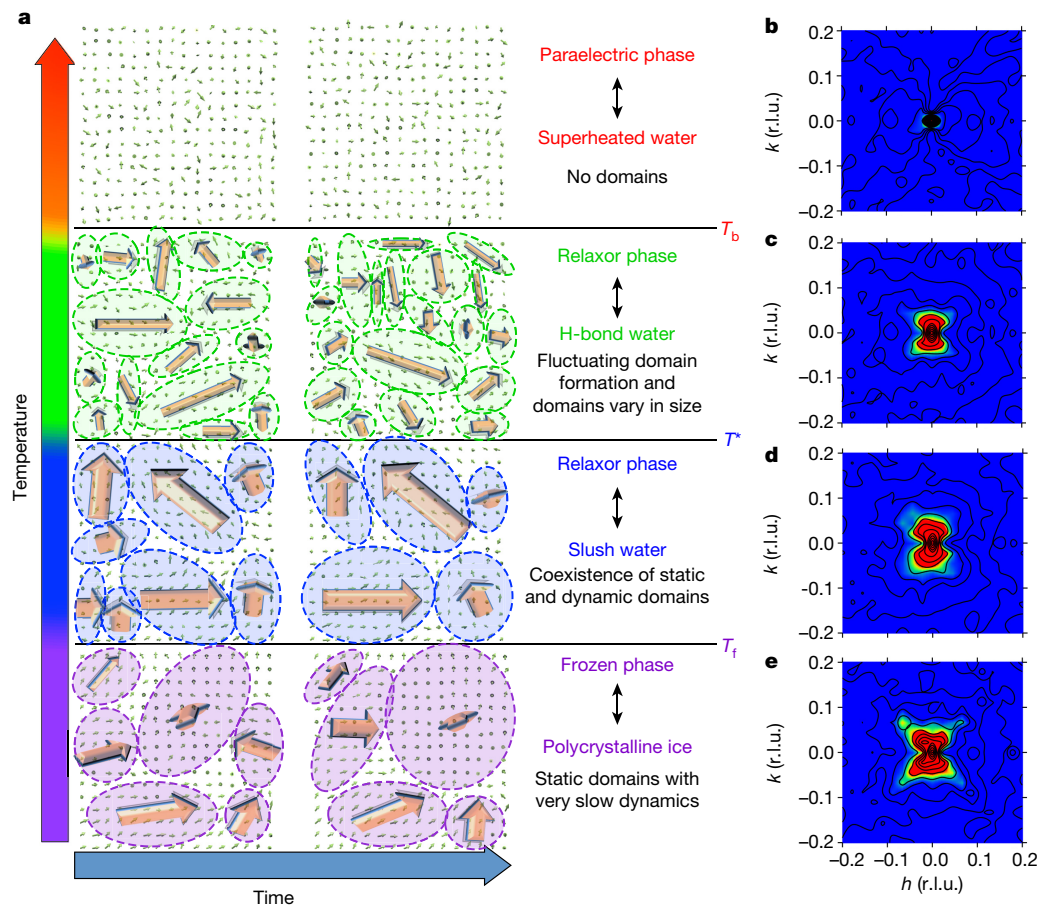


Figure 2 | Schematic of our slush-like model for the phase transitions in relaxors and computational diffuse scattering in the phases.

a, Our model of relaxor structure for the four phases of PMN-PT, using molecular dynamics snapshots. In the paraelectric phase ($T > T_b$; red), dipoles are randomly oriented. In the dynamic relaxor phase ($T^* < T < T_b$; green), a correlated displacement network appears that slows dipole reorientations. The correlated regions and locations change with different directions of P in each snapshot. Note that most of the sites are polar, and the extent of correlated displacements is rather short. For $T_f < T < T^*$ (blue), identifiable domains form, with higher local dipole correlations inside the domain and a high density of small-angle domain walls. However, variation in the direction of P is present inside the domain (or, alternatively, the domain-wall boundaries are diffuse), which enables the rotation of domain polarization. For $T < T_f$ (purple), the correlation and magnitude of P inside each domain become stronger,

in the liquid separating the ice crystals are fast and the small ordered crystals of ice are free to rotate with respect to each other. At T_f , the domain polarizations are largely frozen; however, owing to the presence of unit cells with paraelectric-like behaviour, variation in local P and fluctuations in P in relaxors are greater than those in a typical ferroelectric. We therefore suggest that a slushy multi-domain state is a better conceptual framework for describing relaxor structure (Fig. 2a).

We attribute the changes in the diffuse scattering patterns on cooling to changes in the angle correlation. In the paraelectric phase at $T > T_b$, the multi-domain state and the butterfly shape in the diffuse scattering pattern are entirely absent (Fig. 2b). At 500 K, both the diffuse scattering and the multi-domain structure are faint (Fig. 2c). At 400 K, the shapes in the diffuse scattering pattern are slightly more pronounced (Fig. 2d), corresponding to the greater distinction between, within and beyond one domain. As the system undergoes the freezing relaxor transition at T_b , the correlation inside the domains increases, leading to a clearly butterfly pattern (Fig. 2e) and a rapid increase in the diffuse scattering intensity below 400 K (Extended Data Fig. 4b).

but the domain size does not change. The domain walls are sharper and domain P rotates slightly on approximately 1-ns timescales. Approximate domain boundaries are shown by dashed lines; arrow direction and size corresponds to those of P in each domain. The multi-domain structures for $T < T_b$ are similar to the fixed-size polar domains observed for water. **b–e**, Diffuse scattering patterns around the (100) Bragg spot, obtained from our molecular dynamics simulations in the four phases of PMN-PT. Blue, green and red colours show a logarithmic change in intensity of $\leq 10^{-6}$, 5×10^{-6} and $\geq 10^{-5}$, respectively, with 20 constant-intensity contours of the change (corresponding to values of 10^{-11} to 0.25) shown by black lines. No butterfly shape is observed in the paraelectric phase (**b**); the butterfly shape appears in the relaxor phase (**c**); and it becomes stronger and changes shape in the static, frozen phases (**d**, **e**). r.l.u., reciprocal lattice unit.

To confirm our interpretations, we examine the diffuse scattering patterns for several model structures for wave vectors $q = (q_x, q_y)$ with q_x and q_y varying from -0.2 to 0.2 reciprocal lattice units on $(hk0)$ around the (100) Bragg spot. We find that only a multi-domain structure with a degree of disorder for the displacements inside 4-nm domains can exhibit a diffuse scattering pattern that is similar to the molecular-dynamics-obtained butterfly shape (see Extended Data Figs 6, 7 and Methods section ‘Diffuse scattering’). A small domain size is crucial for the experimental¹⁸ and our computed diffuse scattering, because increased domain size rapidly reduces the q -space extent of the diffuse scattering pattern (Extended Data Fig. 7). Therefore, for $T < T_c$, in a normal ferroelectric such as $\text{Pb}(\text{Zr,Ti})\text{O}_3$, with large (> 100 nm) domain sizes that grow as a result of dipole couplings on cooling, diffuse scattering has not been observed experimentally. In contrast, at temperatures just above T_c , the size of correlated domains in $\text{Pb}(\text{Zr,Ti})\text{O}_3$ is small, giving rise to the observed diffuse scattering signal. Consequently, we find that the butterfly shape in the diffuse scattering pattern is a signature of a multi-domain ferroelectric state with an extremely high density of low-angle domain walls, one that

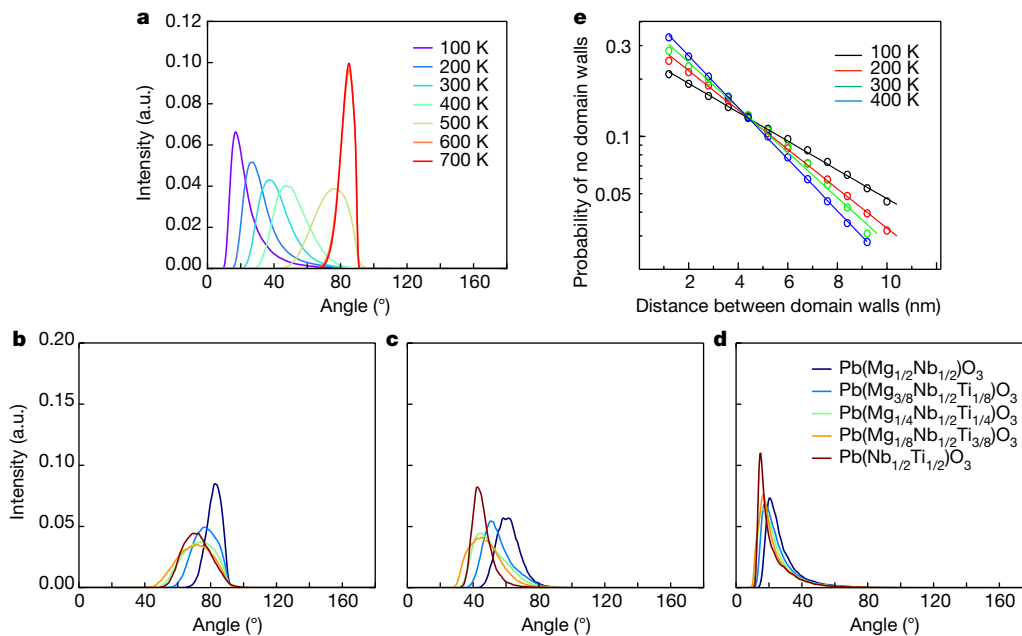


Figure 3 | Autocorrelation function for time-delay-averaged angles between displacements of Pb atoms. **a**, Autocorrelations for Pb atoms in the entire PMN-PT crystal at various T . The distribution of the autocorrelation is similar to that of the local tetrahedral order parameter in water, as obtained²³ using molecular dynamics simulations. **b–d**, Autocorrelations of Pb atoms in subgroups based on their eight nearest B-cation neighbours at 500 K (**b**), 400 K (**c**) and 100 K (**d**). The integrated intensities of all functions are normalized to unity for a clearer

requires neither a non-polar matrix nor the marked growth of domain size below T^* to produce the high diffuse scattering intensity, even at temperatures below T_f .

We investigate the formation of small domains and the degree of slush-like disorder by analysing the influence of the local environment on the Pb displacements using the distribution of time-delay-averaged angle autocorrelation. We decompose the total distribution function into the contributions from Pb atoms in five subgroups with different B-cation nearest neighbours in ‘random-site’ rocksalt-ordered PMN-PT²⁷ (Extended Data Fig. 9a, b). In Fig. 3b–d, we present the distributions for each subgroup in our PMN-PT at different temperatures.

The relatively low angle at the peak intensity for the $\text{Pb}(\text{Nb}_{1/2}\text{Ti}_{1/2})\text{O}_3$ cells in Fig. 3b indicates that the dipole rotations in these cells start to slow down already at 500 K. However, the substantial skewness of the peak reveals that the ferroelectric-like dipole correlation behaviour in these cells is suppressed by the coupling to the neighbouring unit cells of other compositions. This coupling results in the weak diffuse scattering intensity at 500 K despite the presence of the large local Pb displacements below T_b for pure $\text{Pb}(\text{Mg}_{1/3}\text{Nb}_{2/3})\text{O}_3$ (ref. 7) and PMN-PT¹⁷. In Fig. 3c we show that unit cells with paraelectric, ferroelectric and intermediate behaviours are all present at 400 K, indicating the ferroelectric–paraelectric crossover at the sub-nanometre scale. At 300 K, the peak for the paraelectric-like Mg-rich cells shifts to smaller angles, indicating the phase transition at T_f , with the slowing of the dynamic fluctuations similar to what we observe for the Ti-rich cells at 500 K. For temperatures further below the transition at T_f , all cell types show slower rotations, with narrower peaks located at lower angles (Fig. 3d), even though the Mg-rich subgroups exhibit broader peaks that indicate greater disorder. Nevertheless, the distinctive behaviours of the different one-unit-cell Pb environments lead to the presence of disorder inside the polar domains even at low T . The phase transitions are clearly observed in the temperature evolution of the overlap between the angle distribution functions for the Mg- and Ti-rich cells (see Methods section ‘Subgroup perovskite cells’ and Extended Data Fig. 9c).

presentation of their temperature dependence. **e**, Distribution of the probability of no domain walls occurring as a function of the distance between the domain walls, as obtained from our molecular-dynamics-simulated structures. The probability follows a Poisson distribution, which implies that the rate of domain-wall occurrence ranges from $0.07/a$ to $0.12/a$, where a is the lattice constant of PMN-PT; this is equivalent to mean domain sizes of $8a$ – $14a$ or 3–6 nm. a.u., arbitrary units.

The Mg-rich sites are the cause of the small domain size in PMN-PT, acting as walls that decouple the polarization fluctuations of the neighbouring sites. This hypothesis is supported by the Poisson distribution of the domain sizes (Fig. 3e). Such a distribution is due to the random location of the paraelectric Mg-rich cells, with the Poisson rate constant $\lambda = 0.076$ – 0.12 in good agreement with the probability of the occurrence of an Mg-rich cell in PMN-PT (Extended Data Fig. 9b). Because the dipoles inside the small domains are already highly correlated, it is difficult to rotate the polarization of the entire domain and the multi-domain structure is retained even at low T . The displacement decoupling is due to the creation of underbonded O atoms by the presence of Mg^{2+} , with the small off-centre displacement of Mg^{2+} ions arising from their large size and simple, metal electronic structure.

The slush model of relaxor structure predicts six different physical properties of relaxors. The first one is the appearance of a ferroelectric state at low T when a relaxor is cooled under field. The field-cooling process biases all domains to polarize along the thermodynamically favoured direction specified by the field. In the zero-field-cooling case, the domains are already strongly polarized in different directions and the barrier to electric-field-driven reorientation is too large, so the system remains in the relaxor state. Second, addition of Ti leads to the eventual suppression of relaxor behaviour, whereas lower Ti content increases the strength of the relaxor phase. This is due to the lesser (greater) content of the $\text{Pb}(\text{Mg}_{1/2}\text{Nb}_{1/2})\text{O}_3$ wall sites that make the domain size larger (smaller) as the Ti fraction increases (decreases) and is in agreement with the observed reduction in the q -space extent of the diffuse scattering patterns at higher Ti content¹⁸. Eventually, the increased domain size results in the relaxor undergoing a ferroelectric phase transition. Third, the experimentally reported signatures of the structural phase transitions, such as diffuse scattering, arise from the emergence of domains with dynamically varying location and P orientation at T_b , the nanometre-size, static domains with domain walls near T^* , and the high correlations of the local dipoles at T_f . Fourth, the breaking up of the system into small domains and the decoupling of fluctuations in P in each domain have been shown

to lead to the Kohlrausch–Williams–Watts dielectric relaxation and to the Vögel–Fulcher characteristics of the dielectric response that is observed in relaxors²⁸. Fifth, the large magnitudes of the polarization that are reached as P fluctuates in the small domains (for $T^* < T < T_b$) create strong local electric fields that smear the ferroelectric transition, resulting in a diffuse phase transition and a temperature dependence of the dielectric constant²⁹. Finally, the ferroelectric domain-wall region exhibits a high permittivity that can greatly enhance the high-frequency intrinsic dielectric response relative to a bulk single-domain material³⁰. The extremely high density of the domain walls and the presence of a mixture of ferroelectric- and paraelectric-like unit cells in relaxors give rise to a greater flexibility for polarization rotations over a wide temperature range and to the ultrahigh piezoelectric response in relaxors. Our findings are also consistent with the terpolymer relaxor behaviour that is caused by the random formation of domains by strong and weak pinning¹³. Because relaxors have a high density of domain walls as a result of local dipole decoupling, we propose that new relaxors could be discovered by seeking materials with low local domain-wall energies.

Online Content Methods, along with any additional Extended Data display items and Source Data, are available in the online version of the paper; references unique to these sections appear only in the online paper.

Received 6 September 2016; accepted 9 March 2017.

- Park, S.-E. & Shrout, T. R. Ultrahigh strain and piezoelectric behavior in relaxor based ferroelectric single crystals. *J. Appl. Phys.* **82**, 1804 (1997).
- Mischenko, A. S., Zhang, Q., Whatmore, R. W., Scott, J. F. & Mathur, N. D. Giant electrocaloric effect in the thin film relaxor ferroelectric 0.9PbMg_{1/3}Nb_{2/3}O₃–0.1PbTiO₃ near room temperature. *Appl. Phys. Lett.* **89**, 242912 (2006).
- Bokov, A. A. & Ye, Z.-G. Recent progress in relaxor ferroelectrics with perovskite structure. *J. Mater. Sci.* **41**, 31–52 (2006).
- Kutnjak, Z., Petzelt, J. & Blinc, R. The giant electromechanical response in ferroelectric relaxors as a critical phenomenon. *Nature* **441**, 956–959 (2006).
- Scott, J. F. Applications of modern ferroelectrics. *Science* **315**, 954–959 (2007).
- Gehring, P. M., Park, S.-E. & Shirane, G. Soft phonon anomalies in the relaxor ferroelectric Pb(Zn_{1/3}Nb_{2/3})_{0.92}Ti_{0.08}O₃. *Phys. Rev. Lett.* **84**, 5216–5219 (2000).
- Dmowski, W. *et al.* Local lattice dynamics and the origin of the relaxor ferroelectric behavior. *Phys. Rev. Lett.* **100**, 137602 (2008).
- Xu, G., Wen, J., Stock, C. & Gehring, P. Phase instability induced by polar nanoregions in a relaxor ferroelectric system. *Nat. Mater.* **7**, 562–566 (2008).
- Wang, D. *et al.* Fano resonance and dipolar relaxation in lead-free relaxors. *Nat. Commun.* **5**, 5100 (2014).
- Li, F. *et al.* The origin of ultrahigh piezoelectricity in relaxor-ferroelectric solid solution crystals. *Nat. Commun.* **7**, 13807 (2016).
- Burns, G. & Dacol, F. Glassy polarization behavior in ferroelectric compounds Pb(Mg_{1/3}Nb_{2/3})O₃ and Pb(Zn_{1/3}Nb_{2/3})O₃. *Solid State Commun.* **48**, 853–856 (1983).
- Cohen, R. Materials science: relaxors go critical. *Nature* **441**, 941–942 (2006).
- Yang, L. *et al.* Relaxor ferroelectric behavior from strong physical pinning in a poly(vinylidene fluoride-co-trifluoroethylene-co-chlorotrifluoroethylene) random terpolymer. *Macromolecules* **47**, 8119–8125 (2014).
- Bosak, A., Chernyshov, D., Vakhrushev, S. & Krisch, M. Diffuse scattering in relaxor ferroelectrics: true three-dimensional mapping, experimental artefacts and modelling. *Acta Crystallogr. A* **68**, 117–123 (2012).
- Burkovsky, R. *et al.* Structural heterogeneity and diffuse scattering in morphotropic lead zirconate-titanate single crystals. *Phys. Rev. Lett.* **109**, 097603 (2012).
- Phelan, D. *et al.* Role of random electric fields in relaxors. *Proc. Natl Acad. Sci. USA* **111**, 1754–1759 (2014).
- Takenaka, H., Grinberg, I. & Rappe, A. M. Anisotropic local correlations and dynamics in a relaxor ferroelectric. *Phys. Rev. Lett.* **110**, 147602 (2013).
- Matsuura, M. *et al.* Composition dependence of the diffuse scattering in the relaxor ferroelectric compound (1 – x)Pb(Mg_{1/3}Nb_{2/3})O₃–xPbTiO₃ (0 ≤ x ≤ 0.40). *Phys. Rev. B* **74**, 144107 (2006).
- Tinte, S., Burton, B., Cockayne, E. & Waghmare, U. Origin of the relaxor state in Pb(B₁B'_{1–x}) perovskites. *Phys. Rev. Lett.* **97**, 137601 (2006).
- Grinberg, I., Juhás, P., Davies, P. K. & Rappe, A. M. Relationship between local structure and relaxor behavior in perovskite oxides. *Phys. Rev. Lett.* **99**, 267603 (2007).
- Zhang, C. & Galli, G. Dipolar correlations in liquid water. *J. Chem. Phys.* **141**, 084504 (2014).
- Hoffmann, M. M. & Conradi, M. S. Are there hydrogen bonds in supercritical water? *J. Am. Chem. Soc.* **119**, 3811–3817 (1997).
- Guardia, E., Skarmoutsos, I. & Masia, M. Hydrogen bonding and related properties in liquid water: A Car–Parrinello molecular dynamics simulation study. *J. Phys. Chem. B* **119**, 8926–8938 (2015).
- Kumar, P., Buldyrev, S. V. & Stanley, H. E. A tetrahedral entropy for water. *Proc. Natl Acad. Sci. USA* **106**, 22130–22134 (2009).
- Grinberg, I., Shin, Y.-H. & Rappe, A. M. Molecular dynamics study of dielectric response in a relaxor ferroelectric. *Phys. Rev. Lett.* **103**, 197601 (2009).
- Rau, J. G. & Gingras, M. J. P. Spin slush in an extended spin ice model. *Nat. Commun.* **7**, 12234 (2016).
- Akbas, M. A. & Davies, P. K. Domain growth in Pb(Mg_{1/3}Ta_{2/3})O₃ perovskite relaxor ferroelectric oxides. *J. Am. Ceram. Soc.* **80**, 2933–2936 (1997).
- Chamberlin, R. V. The big world of nanothermodynamics. *Entropy* **17**, 52–73 (2014).
- Bokov, A. & Ye, Z.-G. Universal relaxor polarization in Pb(Mg_{1/3}Nb_{2/3})O₃ and related materials. *Phys. Rev. B* **66**, 064103 (2002).
- Xu, R., Karthik, J., Damodaran, A. R. & Martin, L. W. Stationary domain wall contribution to enhanced ferroelectric susceptibility. *Nat. Commun.* **5**, 3120 (2014).

Acknowledgements This work was supported by the ONR under grant N00014-12-1-1033. Computational support was provided by the US DOD through a Challenge Grant from the HPCMO. We thank P. M. Gehring for discussions on his experimental diffuse scattering data and the diffuse scattering method.

Author Contributions H.T., I.G. and A.M.R. designed the simulation approach and analysed the results. The atomistic potential parameters were obtained for small cells by H.T. and S.L., and for larger cells by H.T. H.T. performed the molecular dynamics simulations, and diffuse scattering and correlation function calculations. H.T., I.G. and S.L. made the figures. All authors wrote the paper.

Author Information Reprints and permissions information is available at www.nature.com/reprints. The authors declare no competing financial interests. Readers are welcome to comment on the online version of the paper. Publisher's note: Springer Nature remains neutral with regard to jurisdictional claims in published maps and institutional affiliations. Correspondence and requests for materials should be addressed to H.T. (htakenaka@carnegiescience.edu) and A.M.R. (rappe@sas.upenn.edu).

Reviewer Information *Nature* thanks P. Gehring, G. Guzmán-Verri and the other anonymous reviewer(s) for their contribution to the peer review of this work.

METHODS

Molecular dynamics. Using $36 \times 36 \times 36$ (233,280 atoms), $64 \times 64 \times 64$ (1,310,720 atoms) and $72 \times 72 \times 72$ (1,866,240 atoms) $0.75\text{Pb}(\text{Mg}_{1/3}\text{Nb}_{2/3})\text{O}_3\text{-}0.25\text{PbTiO}_3$ supercells, we perform molecular dynamics (MD) simulations at a range of temperatures from 100 K to 700 K using the bond-valence potential^{31,32} derived from first-principles calculations. We use the first 500 ps of the simulation for equilibration and subsequent 2 ns of simulation time for analysis of the MD data. Because we use the random-site model²⁷ for the B-cation arrangement in PMN-PT, the initial coordinates of our system do not contain the mixture of chemically ordered and chemically disordered regions that were associated with polar nanoregions (PNRs) in previous studies¹⁹.

Diffuse scattering. Using MD simulation results, we obtain the diffuse scattering (DS) intensity, which indicates the deviation of local structure from the average structure, assuming DS is elastic. The DS formula follows the elastic neutron scattering. The neutron scattering intensity $S(\mathbf{Q})$ is defined as square of the magnitude of the neutron wavefunction. The neutron wavefunction $\Psi(\mathbf{Q}, t)$ is

$$\Psi(\mathbf{Q}, t) = \frac{1}{\langle b \rangle} \sum_{i=1}^N b_i e^{-i\mathbf{Q} \cdot \mathbf{R}_i(t)} e^{-|\mathbf{Q}|^2 \sigma_i/4}$$

where N is the number of atoms in the system, b is the neutron scattering length, $\langle b \rangle$ is the average neutron scattering length, \mathbf{Q} is the wavevector, $\mathbf{R}_i(t)$ is the position of atom i as a function of time t and σ_i is the Gaussian width. Because DS intensity cannot appear in an ordered system ($S_{\text{DS}}(\mathbf{Q}) = 0$), we need to subtract the neutron wavefunction for the averaged structure from $\Psi(\mathbf{Q}, t)$. To obtain the averaged structure, we first average each atomic position over time:

$$\mathbf{R}_{t\text{-ave},i} = \frac{1}{t_{\text{tot}}} \int_0^{t_{\text{tot}}} \mathbf{R}_i(t) dt$$

where $\mathbf{R}_{t\text{-ave},i}$ is the time-averaged position of atom i in the system and t_{tot} is the simulation time (2 ns). Second, we calculate position vectors $\mathbf{R}_{\text{hs},i}$, defined as displacements of $\mathbf{R}_{t\text{-ave},i}$ from high-symmetry points, and take the average of the x , y and z components of the position vectors over the whole system:

$$\mathbf{D}_{\text{ave}} = \frac{1}{N} \sum_{i=1}^N (\mathbf{R}_{t\text{-ave},i} - \mathbf{R}_{\text{hs},i})$$

where \mathbf{D}_{ave} is the average displacement vector. Adding \mathbf{D}_{ave} to $\mathbf{R}_{\text{hs},i}$, we obtain the averaged structure $\mathbf{R}_{\text{ave},i} = \mathbf{D}_{\text{ave}} + \mathbf{R}_{\text{hs},i}$. Using $\mathbf{R}_{\text{ave},i}$, the neutron wavefunction $\bar{\Psi}_{\text{ave}}(\mathbf{Q}, t)$ is

$$\bar{\Psi}_{\text{ave}}(\mathbf{Q}, t) = \frac{1}{\langle b \rangle} \sum_{i=1}^N b_i e^{-i\mathbf{Q} \cdot \mathbf{R}_{\text{ave},i}(t)} e^{-|\mathbf{Q}|^2 \sigma_{\text{ave}}/4}$$

where σ_{ave} is the average Gaussian width. Wavevectors \mathbf{Q} at which high peaks of $S(\mathbf{Q})$ appear correspond to Bragg spots. The neutron wavefunction for DS, $\Psi_{\text{DS}}(\mathbf{Q}, t)$, is obtained from $\Psi_{\text{DS}}(\mathbf{Q}, t) = \Psi(\mathbf{Q}, t) - \bar{\Psi}_{\text{ave}}(\mathbf{Q}, t)$. Taking the average of the wavefunction over time,

$$A(\mathbf{Q}) = \frac{1}{t_{\text{tot}}} \int_0^{t_{\text{tot}}} \Psi_{\text{DS}}(\mathbf{Q}, t) dt$$

we obtain the DS intensity $S_{\text{DS}}(\mathbf{Q}) = A^*(\mathbf{Q})A(\mathbf{Q})$, where the asterisk denotes the complex conjugate, which corresponds to time-delay-averaged (static) intensity. The dynamic scattering intensity at frequency ω ,

$$S(\mathbf{Q}, \omega) = \frac{1}{t_{\text{tot}}^2} \iint \Psi^*(\mathbf{Q}, t) \Psi(\mathbf{Q}, t + t') dt e^{i\omega t'} dt' \quad (1)$$

can be rewritten as

$$S(\mathbf{Q}, \omega) = \frac{1}{t_{\text{tot}}} \int \Psi^*(\mathbf{Q}, t) e^{i\omega t} dt \times \frac{1}{t_{\text{tot}}} \int \Psi(\mathbf{Q}, t') e^{-i\omega t'} dt'$$

with $S(\mathbf{Q}, 0) \equiv S_{\text{DS}}(\mathbf{Q}) = A^*(\mathbf{Q})A(\mathbf{Q})$, where $\Psi = \Psi_{\text{DS}}$, representing elastic scattering, and can greatly reduce computational effort compared with using equation (1).

The DS shows time-delay-averaged (static) deviation from the averaged structures (deviation of Bragg spots in scattering intensity). Therefore, DS intensities cannot appear in a system with simply oscillating or random dynamics, owing to cancellation in averaging of structures over the time delay.

Because the size of the PMN-PT supercell used here is too small to represent the whole crystal, we assume that the supercell represents a part of the whole crystal and therefore introduce cubic symmetry in our diffraction pattern calculations.

The DS patterns (displayed in logarithmic contour plots) obtained from our MD simulations show a strong dependence on the size of the simulation supercell, as can be seen from the comparison between the DS at 300 K obtained with $36 \times 36 \times 36$, $64 \times 64 \times 64$ and $72 \times 72 \times 72$ supercells using 100-ps MD trajectories, and compared to the experimental DS for PMN and PMN-10PT¹⁸ (Extended Data Fig. 2). First, we examine the effects of supercell size in our simulations on the DS patterns. We found that whereas the patterns obtained from $12 \times 12 \times 12$ simulations (not shown) did not display anything similar to a butterfly and the $36 \times 36 \times 36$ simulations showed DS patterns that are only roughly similar to the experimental butterfly and rod patterns, greatly improved agreement with experimental DS was obtained for DS calculated using the trajectories of large cell simulations, with these patterns exhibiting the correct butterfly and rod shapes for DS around the (100) and (110) spots. Examining the experimental DS and our computational butterfly shapes, we find a trend with PT content. The bold black curve of the experimental DS pattern for pure PMN (Extended Data Fig. 2d) shows very deep indentations along the vertical left and right sides of the butterfly (moving along $(1+h, k, 0)$ from $h < 0$ to $h > 0$), and the horizontal top and bottom sides of the butterfly (moving along $(1+h, k, 0)$ from $k < 0$ to $k > 0$) have smaller but still noticeable indentations. In PMN-10PT (Extended Data Fig. 2e), this pattern is less distinct, but with the same vertical versus horizontal features. The vertical sides have moderate indentations, whereas the horizontal sides have much smaller indentations. The higher PT content in our system (Extended Data Fig. 2c) further changes the butterfly shape in the same way, with yet smaller indentations in all directions but preserving the comparative sizes: the vertical sides have small indentations, and the horizontal sizes of the MD-calculated DS have even smaller indentations. For further validation, for the rod-like DS around the (110) Bragg peak, we also compared the ratio of the long and short axes of the ellipse to the values obtained in a previous study¹⁸ of PMN-PT. We find that at 300 K, the long-to-short axis length ratio is 1.8, in excellent agreement with the experimental results of 1.8 for PMN-20PT and 1.7 for PMN-30PT. Because this ratio varies from 2.3 for PMN to 1.5 for PMN-40PT, the fact that we get an essentially exact agreement with experiment is notable and indicates that the $72 \times 72 \times 72$ supercells are sufficiently large and correctly capture the structure that gives rise to the experimentally observed DS. Additionally, a close examination of the DS obtained for low temperatures shows the pinching of the rod shape around the (110) Bragg spot that has been experimentally observed in recent X-ray DS results for PMN-PT¹⁴. The fact that our simulations reproduce this fine feature of the DS is another indication that our simulations are accurate. It is clear that even for the $72 \times 72 \times 72$ supercells, we are only starting to obtain DS patterns that are close to converged with respect to supercell size. However, simulations with larger supercells and 2-ns MD trajectories are extremely challenging because simulations using $72 \times 72 \times 72$ supercells (1.8 million atoms) are already at the edge of current computational capabilities.

We use the structures from our 2-ns $72 \times 72 \times 72$ -supercell MD trajectories to create contour plots of computational DS intensities from -0.2 to 0.2 around (100) and (110) in reciprocal lattice units for 100 K, 200 K, 300 K, 400 K, 500 K, 600 K and 700 K (Extended Data Fig. 3). As the temperature is lowered, DS intensities around (100) emerge, broaden along orthogonal directions giving rise to the butterfly shape, and are preserved at low temperatures (Extended Data Fig. 3a–g). Similarly, the DS intensities around (110) show the trend of forming an ellipsoid-like shape that extends along $(1\bar{1}0)$ (Extended Data Fig. 3h–n). In addition, similarly to the experimental reports, the DS patterns at $T > T_b$ exhibit a bow-tie shape around the (100) and (110) spots.

We examine the temperature evolution of the DS using the same method as in previous experimental studies. Experimental DS studies of relaxors have typically presented the plots of the DS intensity along the (110) direction for both the (100) and (110) Bragg spots. We then fitted this profile using the method in ref. 18 to extract the changes in the integrated intensity I_0 with temperature and composition. A comparison of DS data for PMN, PMN-10PT and PMN-20PT¹⁸ forms a natural basis for comparison with our MD results obtained for PMN-25PT. We plot the obtained DS intensity versus q together with the experimental data for PMN, PMN-10PT and PMN-25PT at 300 K in Extended Data Fig. 4a, and our result clearly follows the trend of the peak widths: the peak is narrower with higher PT content. We then extract I_0 from such plots by fitting a Lorentzian to the high- q ($q > 0.6$) data. The data obtained for I_0 are then compared to the experimental data in Extended Data Fig. 4b. Inspection of the results obtained from MD simulations shows that the temperature evolution of I_0 is similar to that obtained experimentally. Similarly to experimental results, we observe a rapid increase in I_0 slightly below T^* (420 K for PMN and 475 K for PMN-25PT) and a plateau in I_0 at around T_i (200 K for PMN and 350 K for PMN-25PT). A small increase in I_0 is observed below T_b (650 K for PMN and 550 K for PMN-25PT). We also present the plot of the calculated intensity versus wavevector (Extended Data Fig. 4c), which is similar to the experimental data (Extended Data Fig. 4d)³³ for PMN for $T \ll T_b$ (150 K and 350 K).

Next, we examine the relationship between the displacement magnitude and DS intensity. We calculate the DS patterns for a system in which the Pb atoms displace from the centre of O_{12} cages according to the averaged displacements obtained by our MD simulations, with the B cations and O atoms located at the high-symmetry points. To examine the dependence of the DS pattern on the magnitude of Pb displacement, we calculate the DS pattern for the displacements scaled by different factors (Extended Data Fig. 5a–e). Even a reduction in the displacement magnitude by a factor of 5 (corresponding to an average displacement magnitude of 0.01 nm) does not eliminate the butterfly shape, although it does reduce its extent. The DS with the model system reveals that the magnitude of the displacements contributes to the magnitude of the extent along the reciprocal space (110) directions and proves that the stronger DS intensities as T is decreased are due to the large Pb displacements. However, because the scale of the Pb displacements does not influence the DS shape, increased magnitude of the Pb displacements cannot account for the appearance of DS and actual local disorder in PMN–PT. Additionally, the DS pattern obtained using the local displacements normalized to the averaged magnitude of the displacements over the entire system reveals that the butterfly shape does not arise from the fluctuation of the Pb displacement lengths in the supercell (Extended Data Fig. 5f).

We also calculate the DS intensities using model structures with random Pb displacements, ferroelectric (collinear) Pb displacements, ferroelectric Pb displacements with 90° domain walls, and for a structure with dipoles at 20° between the nearest-neighbour cells. These are shown in Extended Data Fig. 6a–d, respectively. Performing Monte Carlo calculations, we generate the structure for Extended Data Fig. 6d in which the nearest-neighbour dipoles form 20° angles, corresponding to the peak height of the dipole–dipole angle correlation at 100 K in Fig. 1a. Here, we use a supercell with 71° domain walls as a model for the DS calculation. We chose this structure because it is easy to model rhombohedral domain walls and because our MD results exhibit domain walls with the form of a multi-domain structure, with angles that are close to 71° . This makes a structure with 71° domain walls a reasonable choice for examining the experimentally observed butterfly shape of the DS pattern. Here as well, the B cations and O atoms are located at the high-symmetry points. The magnitude of the displacements in Extended Data Figs 6 and 7 is the normalized lengths in Extended Data Fig. 5f, and the range of colour contours is the same as in Extended Data Fig. 5. The DS intensities are quite faint in Extended Data Fig. 6a–c and even the DS pattern in Extended Data Fig. 6d does not exhibit the butterfly shape. Consequently, the experimentally observed DS shape cannot be ascribed to these displacement patterns. We then examine the DS patterns for model systems with 71° domain walls and domains of various sizes (Extended Data Fig. 7). Here, the DS pattern exhibits a butterfly-like shape and a clear dependence of DS extent on domain size, with smaller domains giving stronger and more extensive DS patterns. This indicates that the presence of low-angle (for example, 71°) domain walls is essential for the appearance of the experimentally observed butterfly shape in DS.

Angle correlations. For simplicity, we focus our analysis on the correlations in the high-symmetry directions.

First, taking the average over simulation time, we calculate the correlation function of a local dipole for an atomic pair:

$$\alpha_{ij}(t') = \int \hat{D}_i(t) \hat{D}_j(t+t') dt \quad (2)$$

where $\hat{D}_i(t)$ is the unit vector of the off-centre displacement of Pb atom i as a function of time and t' is the time delay. To obtain the angle $\theta_{ij}(t')$ between them from the correlation function, we use

$$\theta_{ij}(t') = \arccos[\alpha_{ij}(t')] \quad (3)$$

The angle correlation distribution is expressed as

$$P_{ij}(\theta, t') = \frac{1}{\sqrt{\pi}\sigma} e^{-[\theta - \theta_{ij}(t')]^2 / \sigma}$$

where θ is a given angle and σ is the Gaussian width. The time-delay-averaged (static) angle correlation distribution function between a Pb atom and Pb atoms in the n th neighbour cell along $\langle 100 \rangle$, $\langle 110 \rangle$ or $\langle 111 \rangle$ directions is given by

$$\frac{1}{N_c N_{\text{pair}}} \sum_{i=1}^{N_c} \sum_{j=1}^{N_{\text{pair}}} \int P_{ij}^{\nu n}(\theta, t') dt'$$

where N_c is the number of Pb atoms in PMN–PT, ν denotes the $\langle 100 \rangle$, $\langle 110 \rangle$ or $\langle 111 \rangle$ direction, n is the neighbour number, and N_{pair} is 6, 12 or 8 for $\nu = \langle 100 \rangle$, $\langle 110 \rangle$ or $\langle 111 \rangle$, respectively.

We analyse the angle correlations between the Pb dipoles along the $\langle 100 \rangle$, $\langle 110 \rangle$ and $\langle 111 \rangle$ directions up to $n = 22$ (Extended Data Fig. 8). For $n > 18$, all of the angle

distributions essentially overlap. Because the angle is calculated using equations (2) and (3), an angle of 90° corresponds to no correlation between the two Pb-atom displacements for temperatures above T_b (Extended Data Fig. 8a–c). In the other words, 90° indicates no coupling between the Pb-atom displacements.

Just below T_b (500 K), in the dynamic relaxor phase, the distributions with peak dispersions as a function of distance are slightly shifted to the left of 90° , with the $n = 1$ distribution showing a noticeably greater shift than those for larger n . (Extended Data Fig. 8d–f). This indicates that the local dipole rotations are not completely uncorrelated, as in the paraelectric phase, because the distributions and their heights are much broader and lower, respectively. The local dipole correlations propagate through neighbour cells. The propagation results in dynamic correlated regions of various sizes. The static features are therefore faint in the entire system, owing not only to the rapid rotations but also to the fluctuation of the correlations that result in the weak DS patterns.

In the relaxor phase, below T^* , the angle correlations clearly show a strong dependence on the distance (Extended Data Fig. 8g–i). As n is increased, the overlap between the distributions increases slowly, at an intermediate rate and rapidly for the $\langle 100 \rangle$, $\langle 110 \rangle$ and $\langle 111 \rangle$ directions, respectively, and the positions of the peaks smoothly from 45° to 70° . The distributions can be distinguished by distance. Examination of the distributions indicates that correlations that signify multi-domain structures are formed for $n < 14$ with fluctuation of the local dipoles inside the domains. For $n > 14$, the low and broadened distributions with a plateau represent the uncorrelated Pb dipole pairs, and the wide range of angles correspond to the formation of vortices.

At 300 K, in the frozen phase, the peaks shift to low angles for $n < 14$ (Extended Data Fig. 8j–l) and the distance trends are similar to those found for 400 K except for the shift. This behaviour indicates that the phase transition from the relaxor phase to the frozen phase is ascribed to the increase in the local order inside the multi-domain structure. The correlations are higher, with essentially no growth of the domain size as T is lowered further. Even in the frozen phase at 100 K, the nearby dipoles are not perfectly aligned, with the low-angle peaks located at 20° for the $\langle 100 \rangle$, $\langle 110 \rangle$ and $\langle 111 \rangle$ directions (Extended Data Fig. 8m–o). Even deep into the frozen phase, high correlation extends only short distances, with $n = 14$ marking the transition between the relative heights of the low-angle (high-correlation) and high-angle (low-correlation) peaks. Whereas the peak position of the low-angle peaks shifts from 55° to 20° as T decreases from 400 K to 100 K, the high-angle peak is consistently located around 60° . This corresponds to the angle between two nearly rhombohedral displacement directions and indicates that the system assumes a multi-domain state, with the small domains separated by domain walls below T^* .

The time-delay-averaged angle autocorrelation distribution function is defined as

$$\frac{1}{N_a} \sum_{i=1}^{N_a} \int P_{ij}(\theta, t') dt'$$

where N_a is the number of Pb atoms in the entire system of PMN–PT for Fig. 3a or in the five subgroups of perovskite cells (see Methods section ‘Subgroup perovskite cells’ below) for Fig. 3b–d.

The time-delay-averaged angle autocorrelation distribution obtained from our MD simulations is shown in Fig. 3a. Because this function measures the magnitude of the local dipole rotation, a small angle indicates ferroelectric behaviour and a large angle indicates paraelectric behaviour. Inspection of Fig. 3a immediately shows the diffuse phase transition in PMN–PT. Above $T_b = 550$ K, extremely fast Pb rotations in the paraelectric phase result in narrow and sharp peaks around 85° . At $T = 500$ K, the marked change in the peak width and height indicate that PMN–PT has undergone the transition to the relaxor phase. At $T = 400$ K, a flat peak can be seen from 45° to 50° . This flat peak is due to the coexistence of the paraelectric- and ferroelectric-like phases. Below T_b , the phase transition from the relaxor phase to the frozen phase occurs, resulting in sharper peaks located at lower angles. Although the phase transition appears to be faint from the data shown in Fig. 3a, a clear signature of the phase transition is observed in the overlap of the autocorrelation distributions of the Ti- and Mg-rich cells, as described in Methods section ‘Subgroup perovskite cells’ below.

Polar nanoregion model. The currently accepted model is deduced from results obtained using several experimental techniques^{11,34–45} and assumes that the relaxor phase is due to the appearance of PNRs inside a non-polar matrix at $T < T_b$. This model was first proposed^{11,34} as a result of the large reduction in the refractive index at T_b . It is also known that the inverse of the dielectric response deviates from the Curie–Weiss law at T_b . As shown in Extended Data Fig. 1, according to the PNR model, these nanoregions increase in size and interact more strongly on cooling, resulting in the appearance of the static local polarizations at T^* (refs 46–49) and eventually the appearance of the frozen phase at T_f , which is a few hundred degrees below T_c for the classic PMN relaxor material.

Several definitions have been suggested for T^* (ref. 50). Following ref. 17, we assign T^* to be the temperature of the sudden increase in the static component of the local off-centre displacement of Pb atoms.

Analysis of domain size. The analysis of local Pb displacements presented in Fig. 1b shows that they are mostly along low-symmetry directions with non-zero values for all three Cartesian polarization components. Pb displacements that are close to the tetragonal (100), orthorhombic (110) and rhombohedral (111) directions are present. In normal ferroelectrics, owing to the restriction of the local orientation of P to the high-symmetry directions, only a few, certain domain walls (and angles) are possible, such as the 180° and 90° domain walls for tetragonal ferroelectric materials. In contrast, in relaxor PMN–PT, the availability of all three high-symmetry states (tetragonal, orthorhombic and rhombohedral) as well as lower-symmetry displacements leads to a wide variety of possible low-angle domain walls. This can be seen in the inset of Fig. 1b, wherein the evolution of P along a line through the supercell shows the large changes in P that are typical of domain walls; however, inspection of these changes shows that rotation of P at the domain wall is typically less than 70° .

To estimate the size of the domains in the $72 \times 72 \times 72$ -supercell PMN–PT system, we used the following procedure. At each temperature, we first calculated the average magnitude of the Cartesian polarization components $P_{i,\text{avg}}$ ($i \in \{x, y, z\}$). For each Cartesian direction i , we evaluate the extent of the domains for the 5,184 one-dimensional slices along that direction by examining $P_{i,k}$ (with $k \in \{1, 2, \dots, 72\}$) for the unit cells along each slice. Starting with $k=1$, we consider the domain to extend until any one of $P_{i,k}$ shows a change equal to $0.7P_{i,\text{avg}}$. The count for the corresponding domain length is then incremented by one and a new domain is considered to start. This procedure is repeated for all 72 unit cells in the one-dimensional slice. The counts for each domain length are then tabulated and their distribution is plotted in Fig. 1b.

Subgroup perovskite cells. As shown in Extended Data Fig. 9a ($6 \times 6 \times 6$ supercell), our simulated PMN–25PT is composed of five different types of Pb-centred perovskite cell. The $\text{Pb}(\text{Nb}_{1/2}\text{Ti}_{1/2})\text{O}_3$ cells rapidly show ferroelectric behaviour on cooling, owing to the high fraction of ferroelectrically active Ti cations. On the other hand, the $\text{Pb}(\text{Mg}_{1/2}\text{Nb}_{1/2})\text{O}_3$ cells exhibit paraelectric behaviour. The number of cells of each type is different owing to the random-site model B-cation arrangement²⁷ (Extended Data Fig. 9b).

Examination of the differences between the correlation functions for the different types of cell clearly shows the relaxor transitions at T_b , T^* and T_f . Here, we plot the overlap between the time-delay-averaged angle autocorrelation distributions for Pb-atom displacements of $\text{Pb}(\text{Mg}_{1/2}\text{Nb}_{1/2})\text{O}_3$ and $\text{Pb}(\text{Nb}_{1/2}\text{Ti}_{1/2})\text{O}_3$ cells as a function of temperature (Extended Data Fig. 9c). To more clearly illustrate the temperature evolution, we multiply the overlap obtained for $T \geq 500$ K by -1 : at high temperatures, all of the distributions are centred around 90° , so a high overlap indicates that all of the local environments are paraelectric-like; in contrast, at low temperature, at which the distribution peaks are located at $\theta < 50^\circ$, a high overlap indicates that all of the local environments are ferroelectric-like. This overlap can therefore be thought of as a measure of the degree of ferroelectricity in the system. Inspection of Extended Data Fig. 9c reveals an initial increase below $T_b = 550$ K that is then followed by a sharp increase until 400 K, which corresponds to the transition into the static relaxor phase at $T^* = 480$ K, and a plateauing at $T < 400$ K, which corresponds to the freezing transition at $T_f = 380$ K.

Similarities of relaxors to water. For comparison of the relaxor dielectric response to that of water, we used the temperature- and frequency-dependent dielectric constant data for water obtained from microwave satellite observations⁵¹. The data are obtained from a fit of experimental data to an expression that contains two independent relaxation processes with non-Arrhenius temperature dependences. The temperature and frequency dependence of the real part of the dielectric constant are shown in Extended Data Fig. 10a. The dielectric response of water resembles that of relaxors. Similarly to relaxors, relaxation at lower frequencies appears at progressively lower temperatures and the temperature of the dielectric constant peak exhibits a non-Arrhenius relationship with frequency (Extended Data Fig. 10b). For frequencies of less than 3 GHz, the dielectric constant ϵ in the weakly relaxing region ($300 \text{ K} < T < 370 \text{ K}$) shows a quadratic Lorentzian dependence on temperature T :

$$\frac{\epsilon_A}{\epsilon} - 1 = \frac{(T - T_A)^2}{2\delta^2}$$

where ϵ_A and T_A are the corresponding frequency-dependent parameters and δ is a frequency-independent coefficient that characterizes the diffuseness of the dielectric constant peak and of the phase transition. Fitting of the curves in Extended Data Fig. 10a reveals that ϵ_A and T_A have a weak dependence on frequency, changing from 147 and 97 K for 0.037 GHz to 118 and 143 K for 1 GHz. This finding is similar to the results⁵² for several relaxor materials; for

example, for PMN–20PT, $T_A = 382$ K and $\epsilon_A = 50 \times 10^3$ at 1 Hz, and $T_A = 385$ K and $\epsilon_A = 44 \times 10^3$ at 100 kHz, with $\delta = 23.7$ K. The similarities between the dielectric response of water and relaxor ferroelectrics were also noted in recent computational studies of water^{53,54}. Despite the similarities, there are some differences between the dielectric response of relaxors and that of water. For example, the value of δ for water is much greater than that for relaxor materials, suggesting a much greater diffuseness of the phase transition. Additionally, although the relationship between the temperature and frequency is non-Arrhenius, it only approximately fits the Vögel–Fulcher formula.

The dynamics and structure of water have long been a subject of intense research, with several recent MD studies elucidating the evolution of local order and hydrogen bonding in water. In particular, the local tetrahedral order parameter has been found to scale linearly with the number of hydrogen bonds, providing a direct link between the structural properties and dipole–dipole correlations²³. The relaxor-like temperature evolution of the ^1H NMR chemical shift²² is therefore a measure of local dipole ordering in water. This link is similar to that between the local Pb displacement magnitude and the local order due to the strong coupling of nearest-neighbour displacements¹⁷. The tetrahedral order parameter distribution $P(Q)$ was also found to exhibit a change from a broad distribution centred on intermediate values of Q at higher temperatures to an asymmetric distribution skewed towards the high- Q values²⁴. This behaviour is quite similar to the temperature evolution of the time-delay-averaged angle autocorrelation function for Pb-atom displacements in the relaxor phase shown in Fig. 3a.

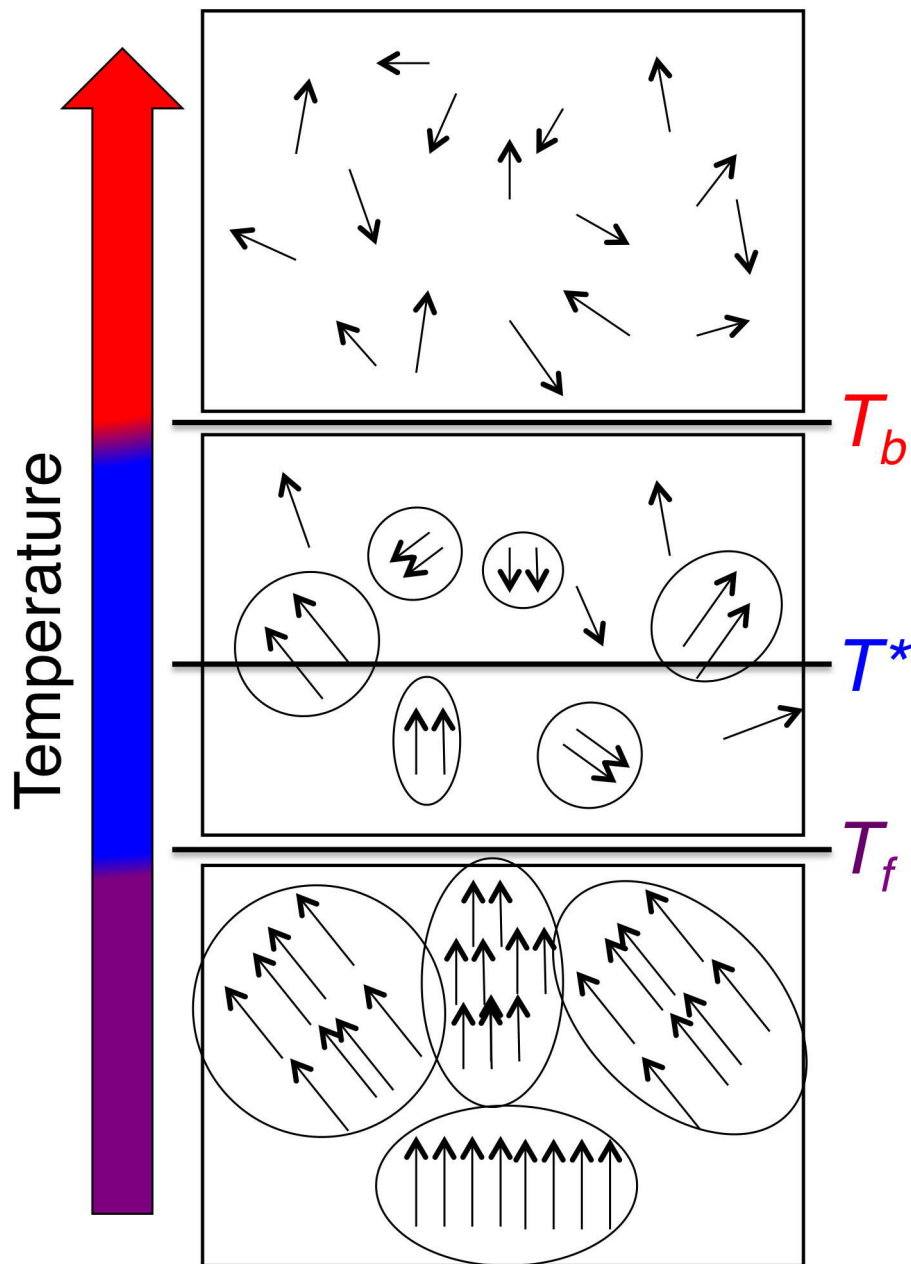
Finally, several recent experimental and theoretical studies of water have found that the region of correlation does not extend past about 1.5 nm. MD simulations of water²¹ have found that the longitudinal dipole–dipole correlation function does not show any changes with temperatures for $r > 1.5$ nm; similar results were obtained in ref. 24.

Experimentally, a high-resolution X-ray diffraction study⁵⁵ showed that the radial pair-distribution function $G_{\text{O-O}}(r)$ for water does not show any temperature changes between 20°C and 63°C past the fourth or fifth coordination shell, whereas the peaks for the first, second and third coordination shells have a strong dependence on temperature, with narrower peaks indicating greater ordering observed at lower T . A similar trend can be deduced from the more extensive, but lower resolution, neutron diffraction results of ref. 56.

Data availability. Data are available from the authors on reasonable request.

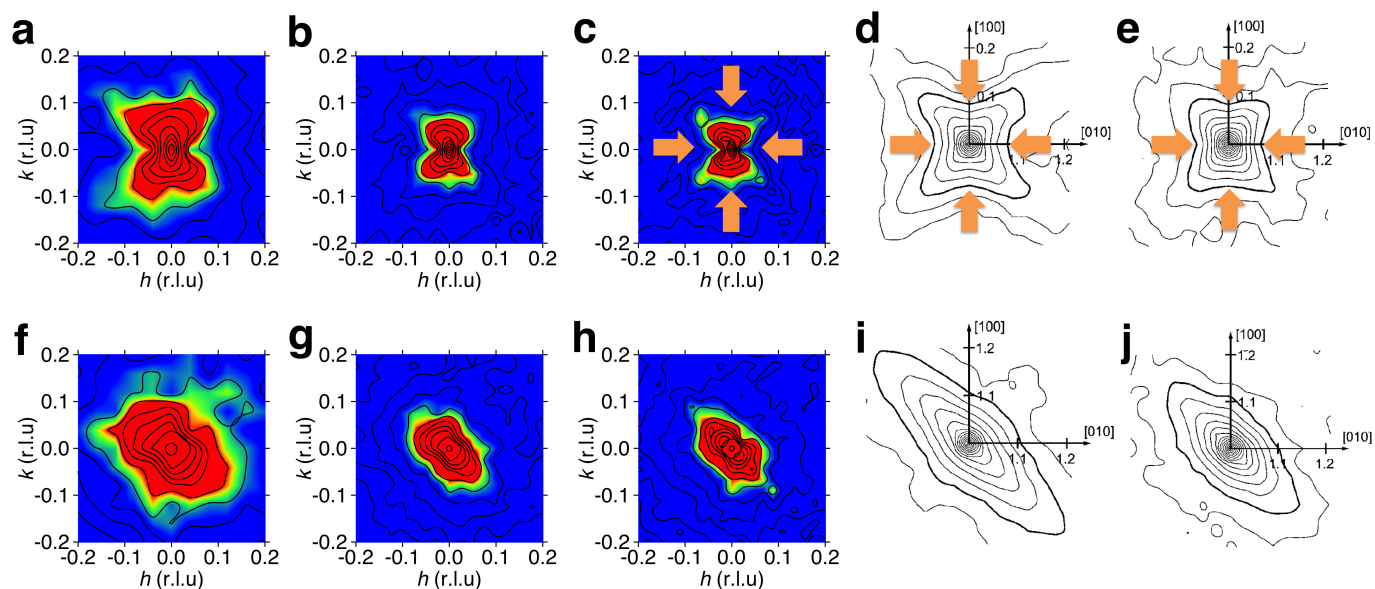
- Shin, Y.-H., Cooper, V. R., Grinberg, I. & Rappe, A. M. Development of a bond-valence molecular-dynamics model for complex oxides. *Phys. Rev. B* **71**, 054104 (2005).
- Liu, S., Grinberg, I., Takenaka, H. & Rappe, A. M. Reinterpretation of the bond-valence model with bond-order formalism: an improved bond-valence-based interatomic potential for PbTiO_3 . *Phys. Rev. B* **88**, 104102 (2013).
- Hiraka, H., Lee, S.-H., Gehring, P., Xu, G. & Shirane, G. Cold neutron study on the diffuse scattering and phonon excitations in the relaxor $\text{Pb}(\text{Mg}_{1/3}\text{Nb}_{2/3})\text{O}_3$. *Phys. Rev. B* **70**, 184105 (2004).
- Burns, G. & Dacol, F. Crystalline ferroelectrics with glassy polarization behavior. *Phys. Rev. B* **28**, 2527–2530 (1983).
- Kirsch, B., Schmitt, H. & Müser, H. Local polarization in PLZT with diffuse phase transition. *Ferroelectrics* **68**, 275–280 (1986).
- Cross, L. E. Relaxor ferroelectrics. *Ferroelectrics* **76**, 241–267 (1987).
- Vakhrušev, S., Kvyatkovsky, B., Naberezhnov, A., Okuneva, N. & Toperverg, B. Glassy phenomena in disordered perovskite-like crystals. *Ferroelectrics* **90**, 173–176 (1989).
- Viehland, D., Jang, S., Cross, L. E. & Wuttig, M. Freezing of the polarization fluctuations in lead magnesium niobate relaxors. *J. Appl. Phys.* **68**, 2916–2921 (1990).
- Viehland, D., Wuttig, M. & Cross, L. E. The glassy behavior of relaxor ferroelectrics. *Ferroelectrics* **120**, 71–77 (1991).
- Viehland, D., Li, J., Jang, S., Cross, L. E. & Wuttig, M. Dipolar-glass model for lead magnesium niobate. *Phys. Rev. B* **43**, 8316–8320 (1991).
- Viehland, D., Jang, S., Cross, L. E. & Wuttig, M. Deviation from Curie-Weiss behavior in relaxor ferroelectrics. *Phys. Rev. B* **46**, 8003–8006 (1992).
- Westphal, V., Kleemann, W. & Glinchuk, M. Diffuse phase transitions and random-field-induced domain states of the “relaxor” ferroelectric $\text{PbMg}_{1/3}\text{Nb}_{2/3}\text{O}_3$. *Phys. Rev. Lett.* **68**, 847–850 (1992).
- Rosenfeld, H. & Egami, T. A model of local atomic structure in the relaxor ferroelectric $\text{Pb}(\text{Mg}_{1/3}\text{Nb}_{2/3})\text{O}_3$. *Ferroelectrics* **150**, 183–197 (1993).
- Pirc, R. & Blinc, R. Spherical random-bond–random-field model of relaxor ferroelectrics. *Phys. Rev. B* **60**, 13470–13478 (1999).
- Pirc, R. & Blinc, R. Vogel-Fulcher freezing in relaxor ferroelectrics. *Phys. Rev. B* **76**, 020101 (2007).
- Blinc, R. *et al.* Local polarization distribution and Edwards-Anderson order parameter of relaxor ferroelectrics. *Phys. Rev. Lett.* **83**, 424–427 (1999).
- Svitelskiy, O., Toulouse, J., Yong, G. & Ye, Z.-G. Polarized Raman study of the phonon dynamics in $\text{Pb}(\text{Mg}_{1/3}\text{Nb}_{2/3})\text{O}_3$ crystal. *Phys. Rev. B* **68**, 104107 (2003).

48. Jeong, I.-K. *et al.* Direct observation of the formation of polar nanoregions in $\text{Pb}(\text{Mg}_{1/3}\text{Nb}_{2/3})\text{O}_3$ using neutron pair distribution function analysis. *Phys. Rev. Lett.* **94**, 147602 (2005).
49. Toulouse, J., Jiang, F., Svitelskiy, O., Chen, W. & Ye, Z.-G. Temperature evolution of the relaxor dynamics in $\text{Pb}(\text{Zn}_{1/3}\text{Nb}_{2/3})\text{O}_3$: a critical Raman analysis. *Phys. Rev. B* **72**, 184106 (2005).
50. Toulouse, J. The three characteristic temperatures of relaxor dynamics and their meaning. *Ferroelectrics* **369**, 203–213 (2008).
51. Meissner, T. & Wentz, F. J. The complex dielectric constant of pure and sea water from microwave satellite observations. *IEEE Trans. Geosci. Remote Sens.* **42**, 1836–1849 (2004).
52. Bokov, A. A. *et al.* Empirical scaling of the dielectric permittivity peak in relaxor ferroelectrics. *Phys. Rev. B* **68**, 052102 (2003).
53. Martin, D. R. & Matyushov, D. V. Dipolar nanodomains in protein hydration shells. *J. Phys. Chem. Lett.* **6**, 407–412 (2015).
54. Elton, D. C. & Fernández-Serra, M.-V. Polar nanoregions in water: a study of the dielectric properties of TIP4P/2005, TIP4P/2005f and TTM3F. *J. Chem. Phys.* **140**, 124504 (2014).
55. Huang, C. *et al.* Wide-angle X-ray diffraction and molecular dynamics study of medium-range order in ambient and hot water. *Phys. Chem. Chem. Phys.* **13**, 19997–20007 (2011).
56. Soper, A. The radial distribution functions of water and ice from 220 to 673 K and at pressures up to 400 MPa. *Chem. Phys.* **258**, 121–137 (2000).



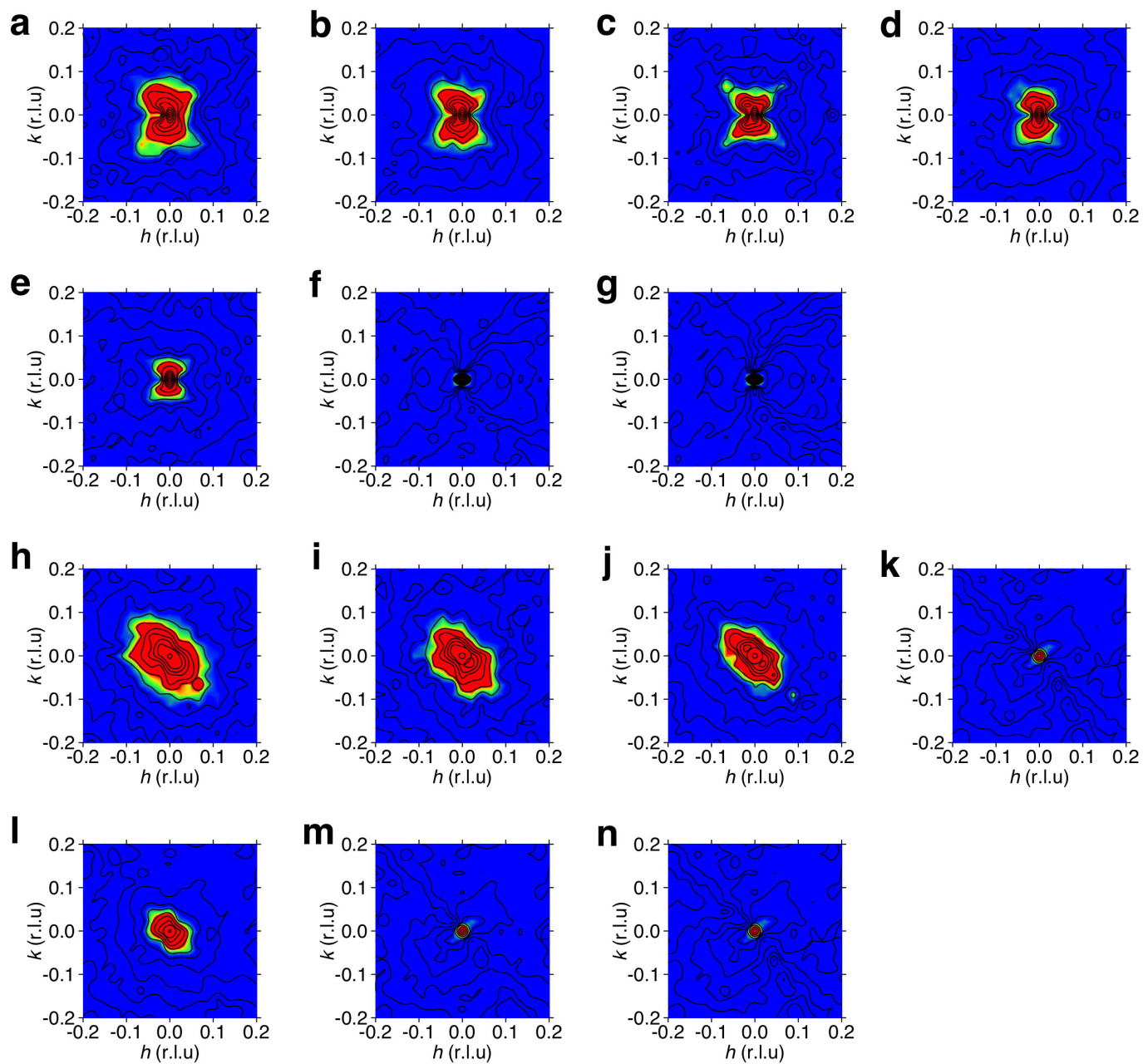
Extended Data Figure 1 | Schematic of the PNR model. In the paraelectric phase, dipoles are randomly oriented (upper panel). At T_b , PNRs appear (middle panel). Dipoles align and are still randomly oriented inside and outside of the PNR. The PNRs grow and interact with each other on cooling. At T^* , roughly halfway between T_b and T_f , static

local distortions were detected using several experimental techniques. As T is lowered further, PNRs coalesce and touch each other and the system undergoes a transition into the frozen phase at T_f (lower panel), in which the PNRs cannot reorient.

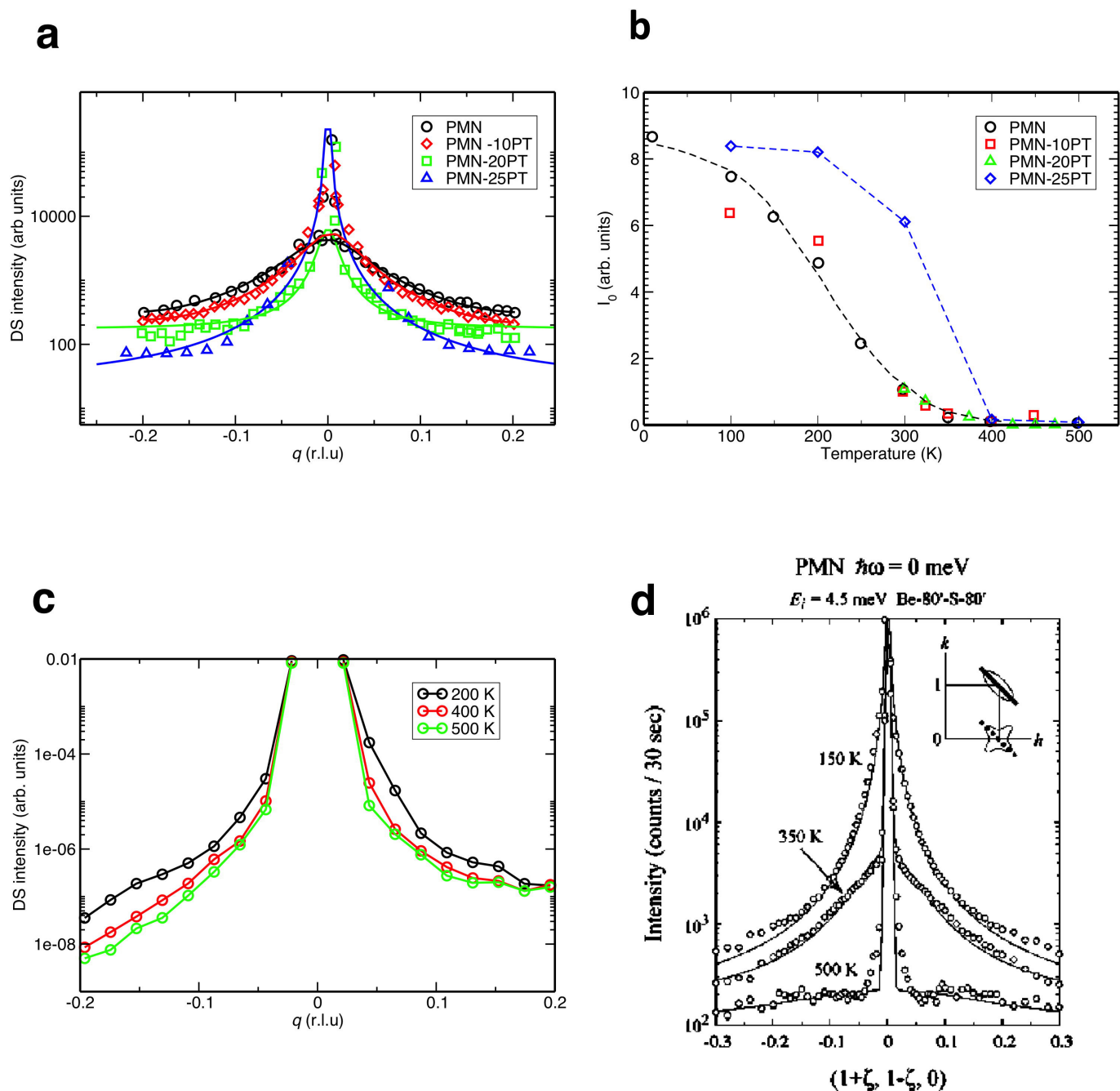


Extended Data Figure 2 | Dependence of DS patterns on the size of MD supercells. We compare our computational DS at 300 K using MD trajectories with 100-ps simulation times to the experimental DS for PMN and PMN-10PT at 300 K (ref. 18). **a–e**, DS around the (100) Bragg spot for $36 \times 36 \times 36$ (**a**), $64 \times 64 \times 64$ (**b**) and $72 \times 72 \times 72$ (**c**) supercells, the

experimental PMN (**d**) and the experimental PMN-10PT (**e**). **f–j**, As **a–e**, but around the (110) Bragg spot. Experimentally reported butterfly and rod shapes can be seen with increasing clarity for larger MD supercells. Orange arrows in **c–e** highlight the changes with PT content. Panels **d**, **e**, **i** and **j** adapted from ref. 18, American Physical Society.

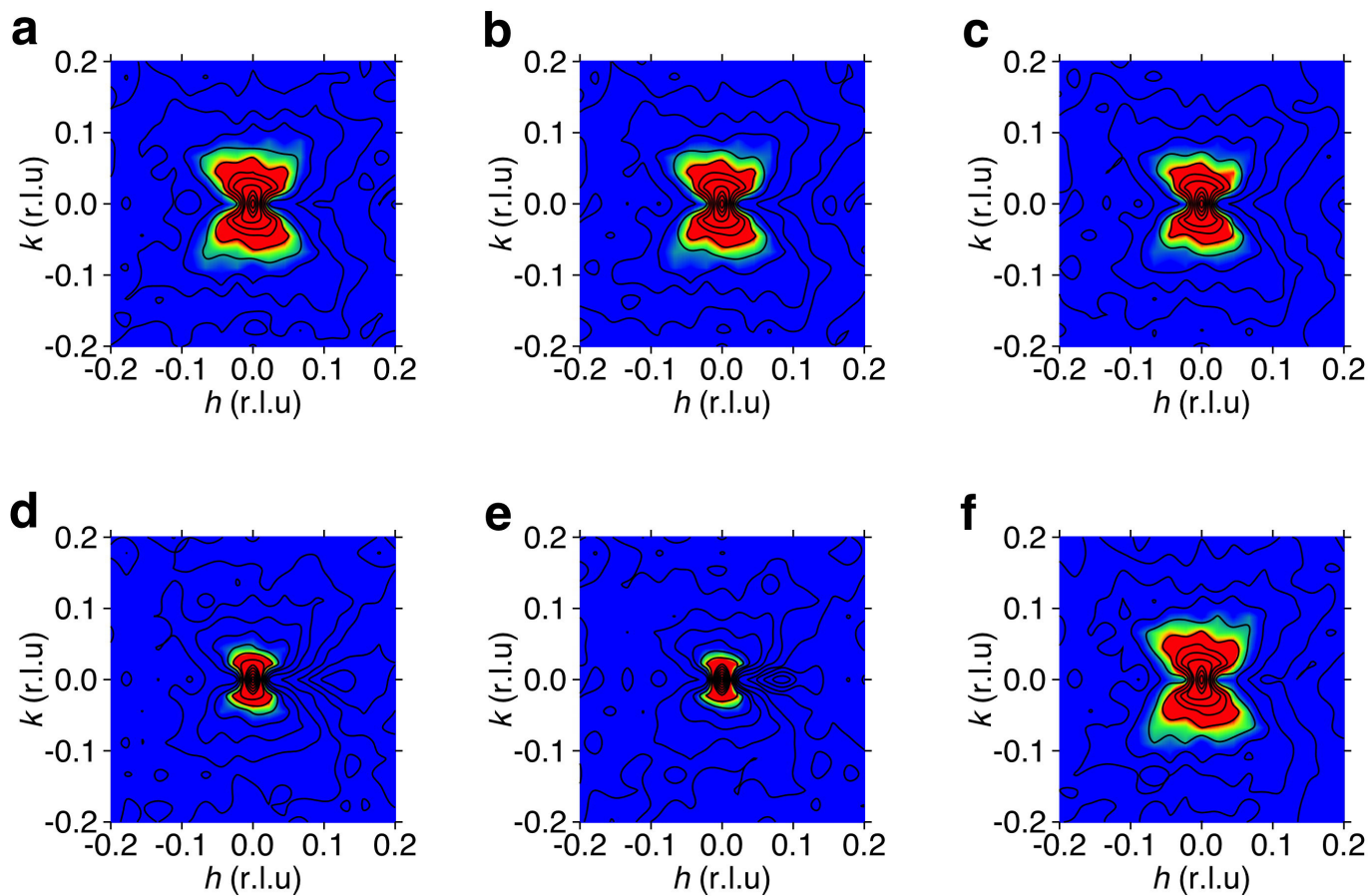


Extended Data Figure 3 | Colour contour plots of the DS. **a–g**, Around (100) at 100 K, 200 K, 300 K, 400 K, 500 K, 600 K and 700 K, respectively. **h–n**, As **a–g**, but around (110).

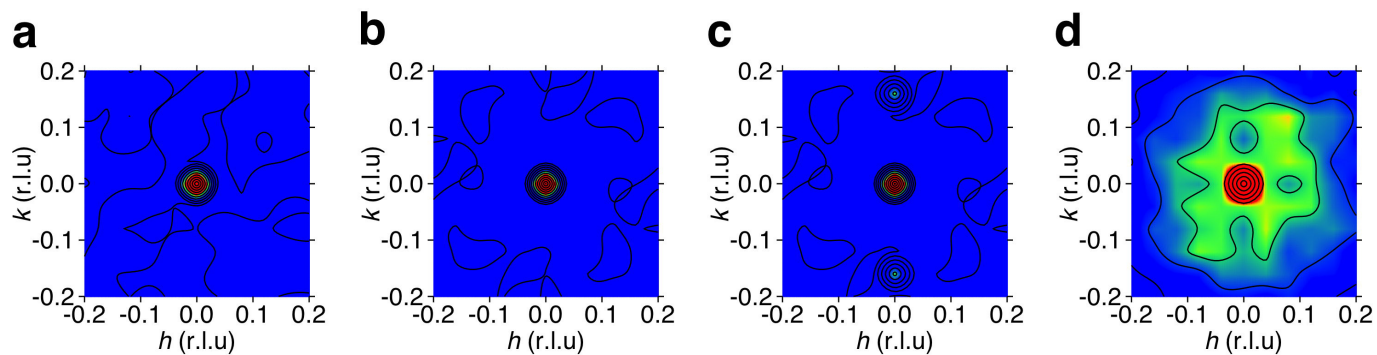


Extended Data Figure 4 | Analysis of the DS intensity of the (110) Bragg spot using scans through q values along the (110) direction, showing the comparison between experimental and theoretical results. a, DS intensity for PMN, PMN-10PT, PMN-20PT (experimental) and PMN-25PT (from MD simulations) at 300 K. b, Temperature dependence

of I_0 extracted by fitting a Lorentzian to the DS intensity. c, d, Temperature dependence of the DS intensity for PMN-25PT (theoretical; c) and PMN (experimental; d)³³. Image in d reproduced with permission from ref. 33, copyright (2004) by the American Physical Society.



Extended Data Figure 5 | DS intensities obtained using time-averaged Pb-atom displacements. a–e, We multiply the lengths of the displacements by 0.9, 0.8, 0.7, 0.3 and 0.2, respectively. **f**, DS intensities obtained using unscaled, time-averaged Pb-atom displacements.

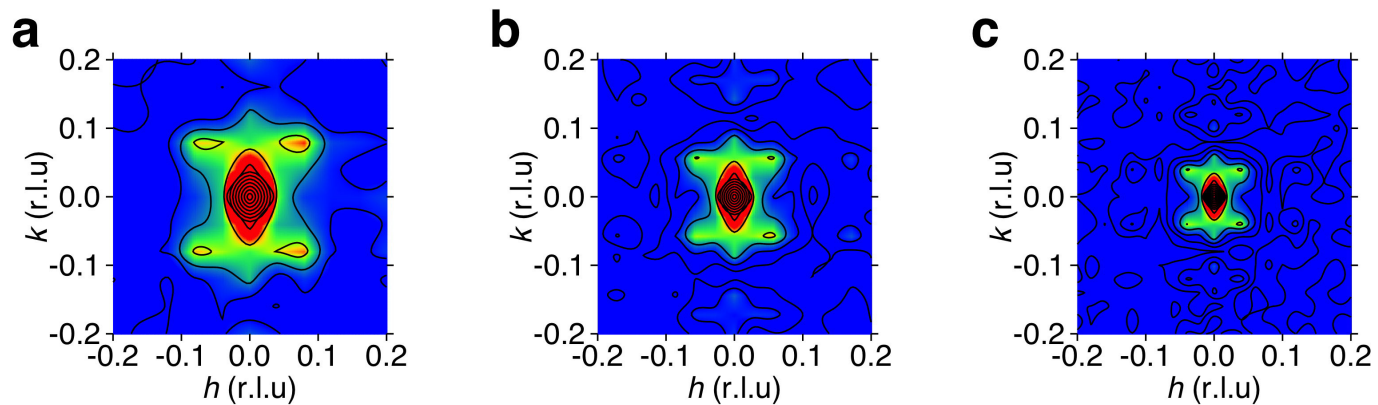


Extended Data Figure 6 | DS intensities using model structures.

a, Paraelectric random displacements. **b**, Ferroelectric collinear displacements. **c**, Ferroelectric displacements with 90° domain walls.

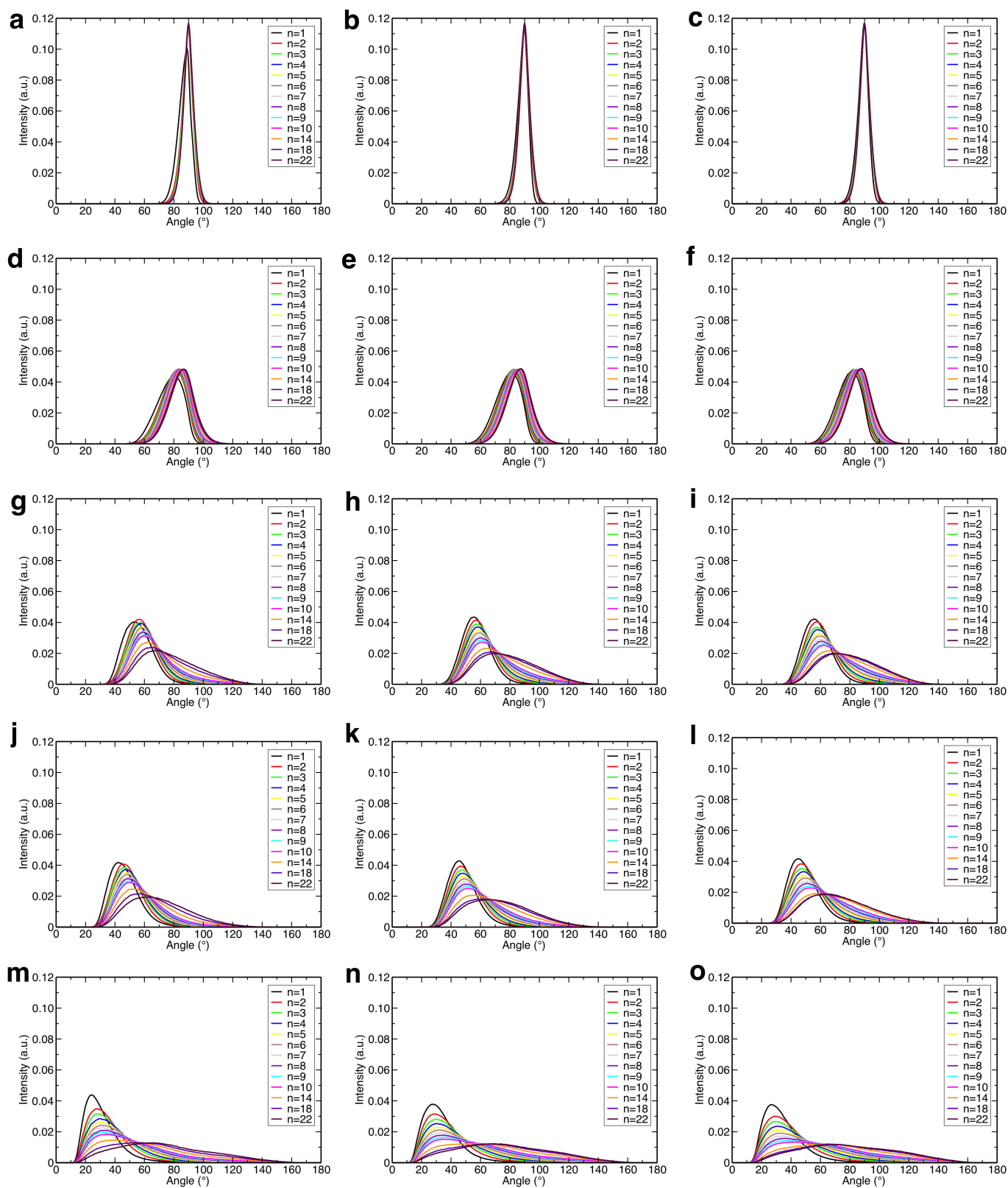
DS intensities are essentially zero for all three models (**a–c**). **d**, A structure

with a 20° angle between dipoles in nearest-neighbour cells obtained by Monte Carlo calculation. In all cases (**a–d**), DS does not assume the butterfly shape.

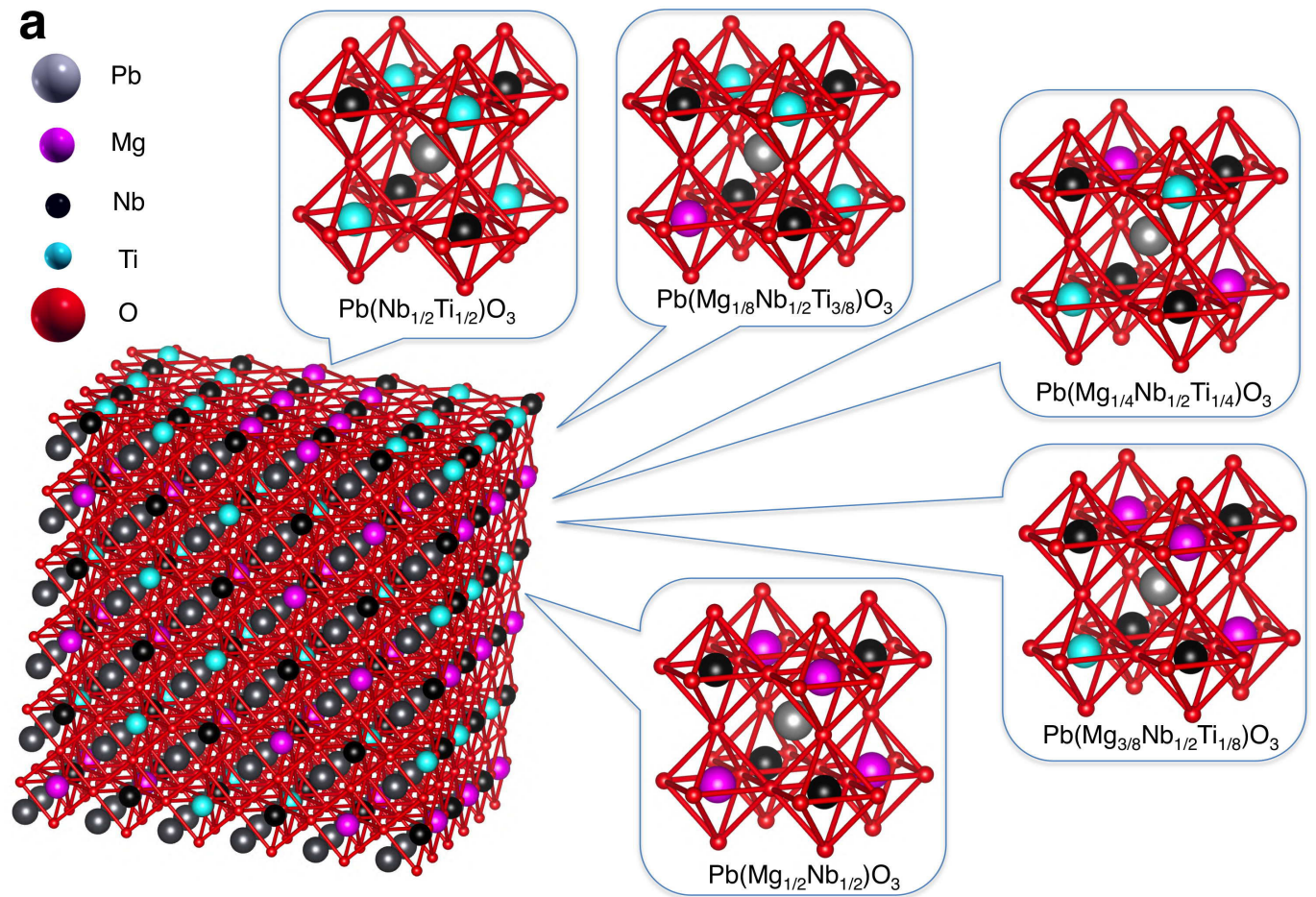


Extended Data Figure 7 | Domain-size dependence of DS intensities for 71° domain-wall model structures. a–c, Domain sizes are 4 nm, 5.6 nm and 8 nm, respectively. As domain size increases, the model butterfly DS pattern shrinks, implying that growth of the correlated domain with

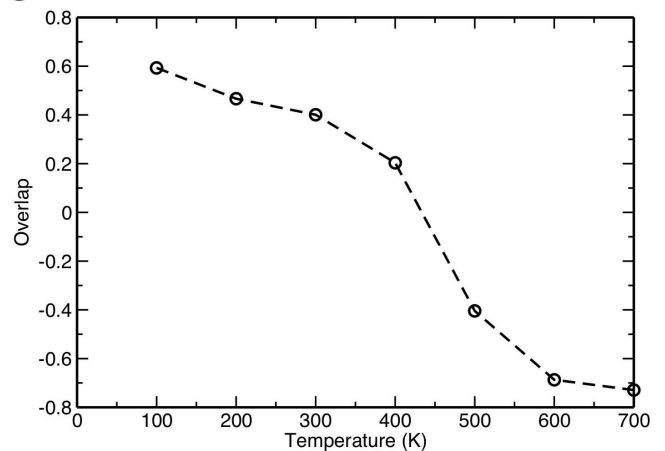
lower temperature would lead to a weaker, less extensive DS pattern, in disagreement with experimental observations of greater DS extent at lower temperatures. However, this observation supports our model of fixed-size domains separated by domain walls.



Extended Data Figure 8 | Time-delay-averaged angle correlation functions for Pb atomic pairs between n th neighbour cells. a–m, Correlations at 600 K (a–c), 500 K (d–f), 400 K (g–i), 300 K (j–l) and 100 K (m–o). Left, middle and right panels correspond to the $\langle 100 \rangle$, $\langle 110 \rangle$ and $\langle 111 \rangle$ directions, respectively.

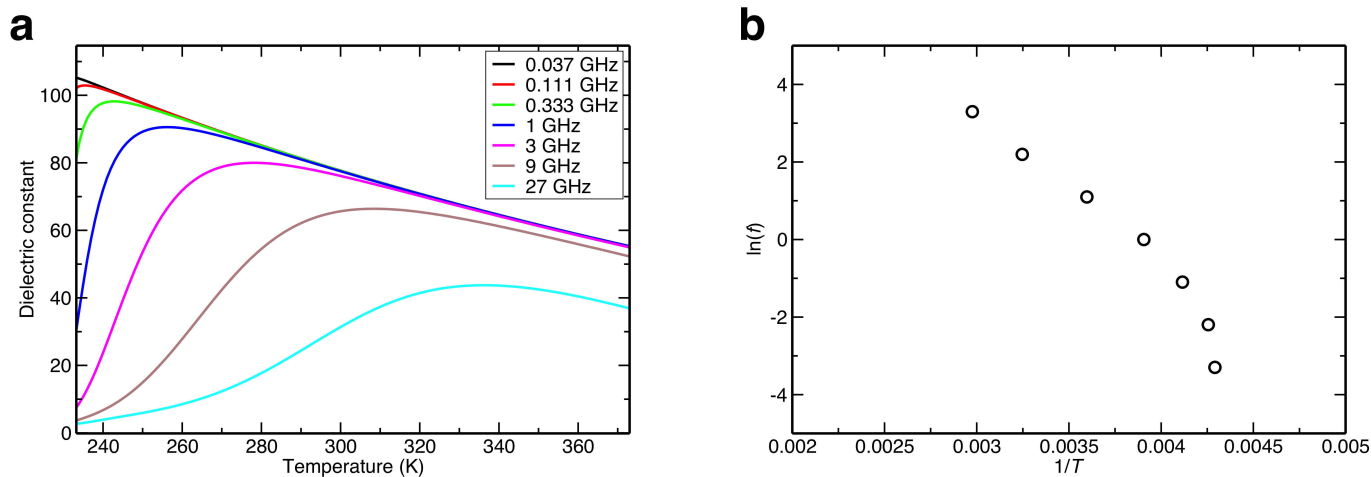
**b**

Subgroup perovskite cells	The number of the cells
$\text{Pb}(\text{Nb}_{1/2}\text{Ti}_{1/2})\text{O}_3$	23197
$\text{Pb}(\text{Mg}_{1/8}\text{Nb}_{1/2}\text{Ti}_{3/8})\text{O}_3$	93349
$\text{Pb}(\text{Mg}_{1/4}\text{Nb}_{1/2}\text{Ti}_{1/4})\text{O}_3$	140255
$\text{Pb}(\text{Mg}_{3/8}\text{Nb}_{1/2}\text{Ti}_{1/8})\text{O}_3$	93151
$\text{Pb}(\text{Mg}_{1/2}\text{Nb}_{1/2})\text{O}_3$	23296

c

Extended Data Figure 9 | Five subgroups of perovskite cells present in PMN-PT. **a**, The five subgroups are illustrated for a $6 \times 6 \times 6$ supercell. **b**, The number of each subgroup in a $72 \times 72 \times 72$ supercell in our MD simulations. **c**, Overlap of time-delay-averaged angle autocorrelation

distributions for Pb-atom displacements in different local environments as a function of temperature. Changes in the temperature dependence of the overlap correspond to the relaxor transition temperatures $T_b = 550$ K, $T^* = 480$ K and $T_f = 380$ K.



Extended Data Figure 10 | Dielectric constant for water. **a**, Real part of the dielectric constant for different frequencies f in the gigahertz range. The frequency dispersion and the diffuseness of the temperature dependence of the dielectric constant are similar to the relaxor dielectric response. **b**, Arrhenius plot of the frequency f as a function of value of the

inverse temperature $1/T$ at which the real part of the dielectric constant is maximum, for the frequencies shown in **a**. A clear non-Arrhenius dependence of frequency on temperature is observed for $f \leq 0.333$ GHz, whereas the plot for the higher f follows the Arrhenius law.